Monthly Notices
of the
ROYAL ASTRONOMICAL SOCIETY

MNRAS **471,** 1259–1279 (2017)
Advance Access publication 2017 April 26

doi:10.1093/mnras/stx998

KiDS-450: testing extensions to the standard cosmological model

Shahab Joudaki,[1,2★] Alexander Mead,[3] Chris Blake,[1] Ami Choi,[4] Jelte de Jong,[5] Thomas Erben,[6] Ian Fenech Conti,[7,8] Ricardo Herbonnet,[5] Catherine Heymans,[4] Hendrik Hildebrandt,[6] Henk Hoekstra,[5] Benjamin Joachimi,[9] Dominik Klaes,[6] Fabian Köhlinger,[5] Konrad Kuijken,[5] John McFarland,[10] Lance Miller,[11] Peter Schneider[6] and Massimo Viola[5]

[1] *Centre for Astrophysics & Supercomputing, Swinburne University of Technology, PO Box 218, Hawthorn, VIC 3122, Australia*
[2] *ARC Centre of Excellence for All-sky Astrophysics (CAASTRO)*
[3] *Department of Physics and Astronomy, The University of British Columbia, 6224 Agricultural Road, Vancouver, B.C. V6T 1Z1, Canada*
[4] *Scottish Universities Physics Alliance, Institute for Astronomy, University of Edinburgh, Royal Observatory, Blackford Hill, Edinburgh EH9 3HJ, UK*
[5] *Leiden Observatory, Leiden University, Niels Bohrweg 2, NL-2333 CA Leiden, the Netherlands*
[6] *Argelander Institute for Astronomy, University of Bonn, Auf dem Hugel 71, D-53121 Bonn, Germany*
[7] *Institute of Space Sciences and Astronomy (ISSA), University of Malta, Msida MSD 2080, Malta*
[8] *Department of Physics, University of Malta, Msida MSD 2080, Malta*
[9] *Department of Physics and Astronomy, University College London, London WC1E 6BT, UK*
[10] *Kapteyn Astronomical Institute, PO Box 800, NL-9700 AV Groningen, the Netherlands*
[11] *Department of Physics, University of Oxford, Denys Wilkinson Building, Keble Road, Oxford OX1 3RH, UK*

Accepted 2017 April 24. Received 2017 April 23; in original form 2016 October 13

ABSTRACT

We test extensions to the standard cosmological model with weak gravitational lensing tomography using 450 deg^2 of imaging data from the Kilo Degree Survey (KiDS). In these extended cosmologies, which include massive neutrinos, non-zero curvature, evolving dark energy, modified gravity and running of the scalar spectral index, we also examine the discordance between KiDS and cosmic microwave background (CMB) measurements from *Planck*. The discordance between the two data sets is largely unaffected by a more conservative treatment of the lensing systematics and the removal of angular scales most sensitive to non-linear physics. The only extended cosmology that simultaneously alleviates the discordance with *Planck* and is at least moderately favoured by the data includes evolving dark energy with a time-dependent equation of state (in the form of the $w_0 - w_a$ parametrization). In this model, the respective $S_8 = \sigma_8\sqrt{\Omega_{\rm m}/0.3}$ constraints agree at the 1σ level, and there is 'substantial concordance' between the KiDS and *Planck* data sets when accounting for the full parameter space. Moreover, the *Planck* constraint on the Hubble constant is wider than in Λ cold dark matter (ΛCDM) and in agreement with the Riess et al. (2016) direct measurement of H_0. The dark energy model is moderately favoured as compared to ΛCDM when combining the KiDS and *Planck* measurements, and marginalized constraints in the w_0–w_a plane are discrepant with a cosmological constant at the 3σ level. KiDS further constrains the sum of neutrino masses to 4.0 eV (95% CL), finds no preference for time or scale-dependent modifications to the metric potentials, and is consistent with flatness and no running of the spectral index.

Key words: gravitational lensing: weak – surveys – cosmology: theory.

1 INTRODUCTION

The weak gravitational lensing measurements of the Kilo Degree Survey (KiDS; de Jong et al. 2013; Kuijken et al. 2015; Fenech-Conti et al. 2017; Hildebrandt et al. 2017) and cosmic microwave background (CMB) measurements of the *Planck* satellite (Planck Collaboration XI 2016a,b) have been found to be substantially discordant (Hildebrandt et al. 2017). When quantifying this discordance in terms of the $S_8 = \sigma_8\sqrt{\Omega_{\rm m}/0.3}$ parameter combination that KiDS measures well (as the amplitude of the lensing measurements roughly scale as $S_8^{2.5}$; Jain & Seljak 1997),

★ E-mail: sjoudaki@swin.edu.au

we find a discordance at the level of 2.3σ (Hildebrandt et al. 2017).

While the area of systematic uncertainties in weak lensing will continue to improve with future studies of KiDS, this discordance is seemingly not resolved even after accounting for intrinsic galaxy alignments, baryonic effects in the nonlinear matter power spectrum and photometric redshift uncertainties, along with additive and multiplicative shear calibration corrections (Hildebrandt et al. 2017). Assuming *Planck* itself is not suffering from an unknown systematic (e.g. Addison et al. 2016; Planck Collaboration LI 2016d), we are therefore motivated to examine to what degree this discordance can be alleviated by an extension to the fiducial treatment of the lensing systematics and by an expansion of the standard cosmological constant + cold dark matter (ΛCDM) model.

Beyond our fiducial treatment of the lensing systematics, which is identical to the approach in Hildebrandt et al. (2017), we consider the impact of a possible redshift dependence in the modelling of the intrinsic galaxy alignments, along with wider priors on the intrinsic alignment amplitude and baryon feedback affecting the non-linear matter power spectrum. We do not consider introducing any free parameters in the modelling of the photometric redshift uncertainties, but instead continue to sample over a large range of bootstrap realizations from our 'weighted direct calibration' (DIR) method that encapsulate the uncertainty in the redshift distribution. Separately, we also examine the discordance between KiDS and *Planck* when taking the conservative approach of discarding all angular bins in the KiDS measurements that are sensitive to nonlinear physics.

In addition to the lensing systematics, the cosmological extensions that we consider are active neutrino masses, non-zero curvature, evolving dark energy (both with a constant equation of state, and with a time-dependent parametrization), modifications to gravity (by modifying the Poisson equation and deflection of light) and non-zero running of the scalar spectral index. We take a conservative approach and consider these extensions independently, but also consider a case where curvature and evolving dark energy are analysed jointly. In our Markov Chain Monte Carlo (MCMC) analyses, we vary the new degrees of freedom of the extended cosmological models along with the standard ΛCDM and lensing systematics parameters (and CMB degrees of freedom when applicable). We list the priors associated with these degrees of freedom in Table 1.

Beyond the KiDS–*Planck* discordance, earlier lensing observations by the Canada–France–Hawaii Telescope Lensing Survey (CFHTLenS; Heymans et al. 2012; Hildebrandt et al. 2012; Erben et al. 2013; Miller et al. 2013) were also found to exhibit a similar tension with *Planck* (e.g. Planck Collaboration XVI 2014; MacCrann et al. 2015; Köhlinger et al. 2016; Planck Collaboration XIII 2016b; Joudaki et al. 2017). This CFHTLenS–*Planck* discordance has been explored in the context of extensions to the standard ΛCDM model and systematic uncertainties in the lensing measurements (e.g. Leistedt, Peiris & Verde 2014; Battye, Charnock & Moss 2015; Dossett et al. 2015; Enqvist et al. 2015; Kunz, Nesseris & Sawicki 2015; MacCrann et al. 2015; Di Valentino, Melchiorri & Silk 2016a; Köhlinger et al. 2016; Liu, Ortiz-Vazquez & Hill 2016; Alsing, Heavens & Jaffe 2017; Joudaki et al. 2017). Meanwhile, lensing observations by the Deep Lens Survey (Jee et al. 2016) exhibit a mild discrepancy with KiDS (at $\sim 1.5\sigma$ in S_8), and observations by the Dark Energy Survey (DES, The Dark Energy Survey Collaborations 2016) have sufficiently large uncertainties that they agree both with CFHTLenS/KiDS and *Planck*.

As we focus on the discordance between KiDS and *Planck* in the context of extended cosmologies, we also examine whether these cosmologies can simultaneously resolve the approximately 3σ tension between *Planck* and local measurements of the Hubble constant based on the cosmic distance ladder (Riess et al. 2011, 2016). In particular, it has been suggested that the tension in the Hubble constant can be resolved by invoking non-standard physics in the dark energy and dark radiation sectors (most recently, e.g. Archidiacono et al. 2016; Bernal, Verde & Riess 2016; Di Valentino, Melchiorri & Silk 2016a,b; Grandis et al. 2016; Karwal & Kamionkowski 2016; Riess et al. 2016).

Beyond questions of data set concordance, we examine to what extent the additional degrees of freedom in the extended cosmological models are constrained by the data (when KiDS and *Planck* are not in tension), and to what degree the extended models are favoured by the data from the point of view of model selection, using statistical tools such as the deviance information criterion (DIC). In assessing the viability of the extended cosmologies, it is not sufficient that they alleviate the discordance with *Planck*, but they need to be favoured by the data from the point of model selection as compared to the standard cosmology.

In Section 2, we describe the KiDS measurements and underlying statistics used to analyse them. In Section 3, we constrain

Table 1. Priors on the cosmological and lensing systematics parameters. The cosmological parameters in the first third of this table are defined as 'vanilla' parameters, and θ_s denotes the angular size of the sound horizon at the redshift of last scattering. We always vary the vanilla parameters and lensing systematics parameters (IA and baryon feedback amplitudes) in our MCMC calculations. Following Hildebrandt et al. (2017), we also always account for photometric redshift uncertainties by using 1000 bootstrap realizations of the tomographic redshift distributions (see Section 2.1). We emphasize that the Hubble constant is a derived parameter. Unlike the analysis in Hildebrandt et al. (2017), we fiducially do not impose an informative prior on the Hubble constant from Riess et al. (2016), and we impose a weaker informative prior on the baryon density, as described in Section 2.1. When we do impose an informative prior on the Hubble constant in specific instances, this is manifested as a uniform $\pm 5\sigma$ prior from Riess et al. (2016), such that $0.64 < h < 0.82$. The optical depth is only varied when the CMB is considered. The extended cosmological parameters are varied as described in Sections 3.2–3.8.

Parameter	Symbol	Prior
Cold dark matter density	$\Omega_c h^2$	[0.001, 0.99]
Baryon density	$\Omega_b h^2$	[0.013, 0.033]
$100 \times$ approximation to θ_s	$100\theta_{MC}$	[0.5, 10]
Amplitude of scalar spectrum	$\ln(10^{10} A_s)$	[1.7, 5.0]
Scalar spectral index	n_s	[0.7, 1.3]
Optical depth	τ	[0.01, 0.8]
Dimensionless Hubble constant	h	[0.4, 1.0]
Pivot scale (Mpc^{-1})	k_{pivot}	0.05
IA amplitude	A_{IA}	[−6, 6]
– *extended case*		[−20, 20]
IA redshift dependence	η_{IA}	[0, 0]
– *extended case*		[−20, 20]
Feedback amplitude	B	[2, 4]
– *extended case*		[1, 10]
MG bins (modifying grav. const.)	Q_i	[0, 10]
MG bins (modifying deflect. light)	Σ_j	[0, 10]
Sum of neutrino masses (eV)	$\sum m_\nu$	[0.06, 10]
Effective number of neutrinos	N_{eff}	[1.046, 10]
Constant dark energy EOS	w	[−3, 0]
Present dark energy EOS	w_0	[−3, 0]
Derivative of dark energy EOS	w_a	[−5, 5]
Curvature	Ω_k	[−0.15, 0.15]
Running of the spectral index	$\mathrm{d}n_s/\mathrm{d}\ln k$	[−0.5, 0.5]

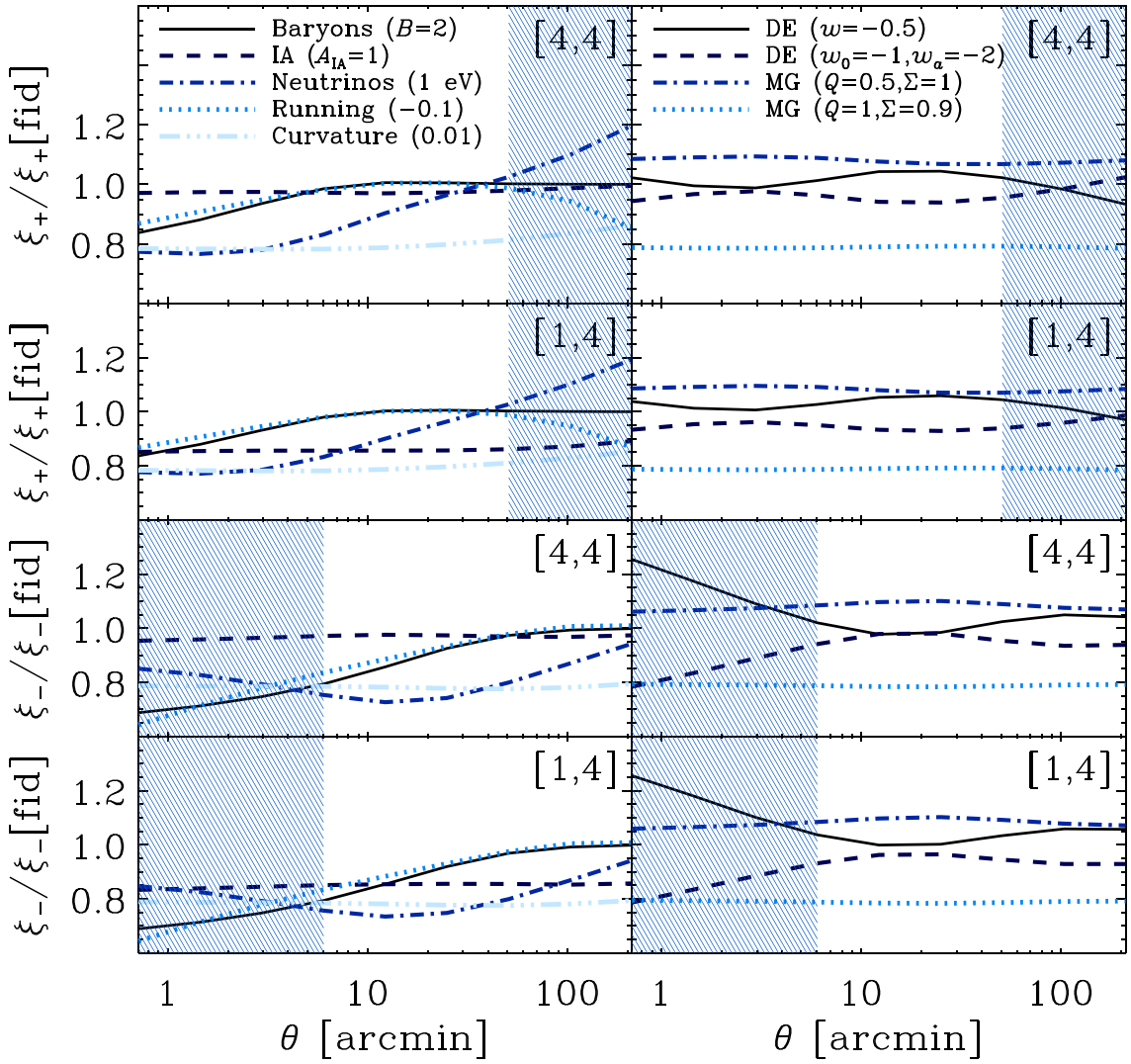

Figure 1. Ratio of shear correlation functions $\xi_{\pm}^{ij}(\theta)$ for tomographic bin combinations $\{1, 4\}$ and $\{4, 4\}$, taken for each extended parameter with respect to a flat ΛCDM model including no systematic uncertainties (denoted as $\xi_{\pm}$[fid]). Parameter definitions are listed in Table 1. For each perturbation, we keep all primary parameters fixed. These primary parameters include $\{\Omega_c h^2, \Omega_b h^2, \theta_{MC}, \ln(10^{10} A_s), n_s\}$, along with the intrinsic alignment amplitude A_{IA} and baryon feedback amplitude B when not explicitly varied (but not for instance the Hubble constant as it is a derived parameter). The curvature case corresponds to $\Omega_k = 0.01$, the neutrino mass case corresponds to $\sum m_\nu = 1$ eV, and the case with non-zero running corresponds to $dn_s/d\ln k = -0.1$. The modified gravity parameters Q and Σ modify the gravitational constant and deflection of light, respectively. The dark energy equation of state can either be constant (w), or possess a time dependence with w_0 and w_a. The shaded regions correspond to angular scales that are masked out in the KiDS analysis.

extensions to the fiducial treatment of the lensing systematics and to the standard cosmological model, in the form of massive neutrinos, curvature, evolving dark energy, modified gravity (MG) and running of the scalar spectral index. We examine to what degree the extended cosmologies are favoured by KiDS and *Planck*, and to what extent they help to alleviate the ΛCDM discordance between the KiDS and *Planck* data sets. In Section 4, we conclude with a discussion of our results.

2 METHODOLOGY

We give a description of the KiDS and *Planck* data sets used and computational approach in Section 2.1, our statistical analysis tools in Section 2.2 and baseline configurations in Section 2.3.

2.1 Theory and measurements

We follow the approach presented in Hildebrandt et al. (2017) to compute the weak lensing theory and associated systematic uncertainties, using the same KiDS-450 cosmic shear tomography measurements, redshift distributions, analytic covariance matrix and cosmology fitting pipeline.

The lensing observables are given by the two-point shear correlation functions $\xi_{\pm}^{ij}(\theta)$, for tomographic bin combination $\{i, j\}$ at angle θ (e.g. see equations 2–5 in Hildebrandt et al. 2017). The KiDS-450 data set (Kuijken et al. 2015; Fenech-Conti et al. 2017; Hildebrandt et al. 2017) covers an effective area of 360 deg^2, with a median redshift of $z_m = 0.53$, and an effective number density of $n_{eff} = 8.5$ galaxies arcmin^{-2}. The raw pixel data is processed by THELI (Erben et al. 2013) and ASTRO-WISE (Begeman et al. 2013; de Jong et al. 2015), while the shears are measured using *lens*fit

Table 2. Exploring changes in $\chi^2_{\rm eff}$ and DIC for different extensions to the standard cosmological model (given the priors in Table 1, lensing systematics always included). The reference ΛCDM model (with fiducial treatment of lensing systematics) gives $\chi^2_{\rm eff} = 162.3$ and DIC = 177.4 for KiDS (marginally different from the values in Hildebrandt et al. 2017 due to wider priors on the baryon density and Hubble constant), $\chi^2_{\rm eff} = 11265.4$ and DIC = 11297.5 for *Planck* (marginal change from Planck Collaboration XIII 2016b due to different priors), $\chi^2_{\rm eff} = 11438.6$ and DIC = 11477.8 for the joint analysis of KiDS and *Planck*, $\chi^2_{\rm eff} = 11439.0$ and DIC = 11478.0 for the joint analysis of KiDS and *Planck* with an informative Hubble constant prior from Riess et al. (2016). Negative values indicate preference in favour of the extended model as compared to fiducial ΛCDM.

Model	$\Delta\chi^2_{\rm eff}$	ΔDIC
ΛCDM (extended systematics)		
– *KiDS*	−2.1	2.4
– *Planck*	0	0
– *KiDS+Planck*	−0.87	2.7
Neutrino mass		
– *KiDS*	0.10	2.7
– *Planck*	2.0	3.4
– *KiDS+Planck*	2.9	3.3
Curvature		
– *KiDS*	−0.96	−0.22
– *Planck*	−5.8	−4.3
– *KiDS+Planck*	−0.22	0.31
Dark energy (constant w)		
– *KiDS*	0.074	2.3
– *Planck*	−3.1	−0.20
– *KiDS+Planck*	−5.5	−5.4
– *KiDS+Planck*+H_0	−3.4	−2.9
Dark energy ($w_0 - w_a$)		
– *KiDS*	−0.35	0.95
– *Planck*	−3.2	−1.1
– *KiDS+Planck*	−6.4	−6.8
– *KiDS+Planck*+H_0	−6.5	−6.4
Curvature + dark energy (constant w)		
– *KiDS*	−0.44	0.30
– *Planck*	−6.2	−3.7
– *KiDS+Planck*	−5.8	−3.6
– *KiDS+Planck*+H_0	−3.6	−2.0
Modified gravity (fiducial scales)		
– *KiDS*	−3.6	−0.094
– *Planck*	−4.0	5.7
– *KiDS+Planck*	−4.2	0.77
Modified gravity (large scales)		
– *KiDS*	−6.4	5.9
– *Planck*	−4.0	5.7
– *KiDS+Planck*	−6.5	2.4
Running of the spectral index		
– *KiDS*	−1.1	0.27
– *Planck*	−0.058	0.68
– *KiDS+Planck*	0.46	1.1

Table 3. Assessing the level of concordance between KiDS and *Planck* as quantified by $T(S_8)$ defined in equation (2), and $\log\mathcal{I}$ (base 10) defined in equation (3). The ΛCDM results with fiducial treatment of the systematic uncertainties differ marginally from Hildebrandt et al. (2017) due to our wider priors on the Hubble constant and baryon density.

Model	$T(S_8)$	$\log\mathcal{I}$
ΛCDM		
— fiducial systematics	2.1σ	−0.63
— extended systematics	1.8σ	−0.70
— large scales	1.9σ	−0.62
Neutrino mass	2.4σ	−0.011
Curvature	3.5σ	−1.7
Dark energy (constant w)	0.89σ	0.99
Dark energy ($w_0 - w_a$)	0.91σ	0.82
Curvature + dark energy (constant w)	2.5σ	−0.59
Modified gravity (fiducial scales)	0.49σ	0.42
Modified gravity (large scales)	0.83σ	1.4
Running of the spectral index	2.3σ	−0.66

(Miller et al. 2013). The data set consists of four tomographic bins between $z_{\rm B} = 0.1$ and $z_{\rm B} = 0.9$ (equal widths $\Delta z_{\rm B} = 0.2$), where $z_{\rm B}$ is the best-fitting redshift output by BPZ (Benítez 2000). For each tomographic bin, the measurements cover seven angular bins between 0.5 and 72 arcmin in $\xi_+^{ij}(\theta)$ and six angular bins logarithmically spaced between 4.2 and 300 arcmin in $\xi_-^{ij}(\theta)$. In other words, considering nine angular bins with central values at [0.713, 1.45, 2.96, 6.01, 12.2, 24.9, 50.7, 103, 210] arcmin, the last two angular bins are masked out for $\xi_+^{ij}(\theta)$ and the first three angular bins are masked out for $\xi_-^{ij}(\theta)$. This equates to a total of 130 elements in our data vector. We use an analytical model that accounts for both Gaussian and non-Gaussian contributions in calculating the covariance matrix of our data, as described in Hildebrandt et al. (2017, further see Joachimi et al., in preparation).

Given external overlapping spectroscopic surveys, we calibrate the photometric redshift distributions using the 'weighted direct calibration' (DIR) method in Hildebrandt et al. (2017), with uncertainties and correlations between tomographic bins obtained from 1000 bootstrap realizations (using each bootstrap sample for a fixed number of MCMC iterations). We account for intrinsic galaxy alignments, given by correlations of intrinsic ellipticities of galaxies with each other and with the shear of background sources, by varying an unknown amplitude $A_{\rm IA}$ and redshift dependence $\eta_{\rm IA}$ (e.g. see equations 4–7 in Joudaki et al. 2017). As a result, the 'shear-intrinsic' and 'intrinsic-intrinsic' power spectra are proportional to $A_{\rm IA}(1+z)^{\eta_{\rm IA}}$ and $A_{\rm IA}^2(1+z)^{2\eta_{\rm IA}}$, respectively. Since the mean luminosity is effectively the same across tomographic bins in KiDS, we do not consider a possible luminosity dependence of the intrinsic alignment signal (Hildebrandt et al. 2017). The standard power-law extension for redshift and luminosity were introduced to account for their dependence in the coupling between galaxy shape and tidal field, which is unconstrained in any IA model. A weakness of this extension is that it is purely empirical, but it has been fit to data and demonstrated to work well (e.g. Joachimi et al. 2011). We also do not account for a scale dependence as there is currently no indication for it from data.

We include baryonic effects in the non-linear matter power spectrum with HMCODE (Mead et al. 2015, 2016, now incorporated in CAMB; Lewis, Challinor & Lasenby 2000), which is a new accurate halo model calibrated to the Coyote dark matter simulations (Heitmann et al. 2014, references therein) and the OverWhelmingly Large (OWL) hydrodynamical simulations (Schaye et al. 2010; van Daalen et al. 2011). In HMCODE, the feedback amplitude B is a free parameter that is varied in our analysis. In this one-parameter baryon model, B modifies the halo mass–concentration relation and simultaneously lightly changes the overall shape of the halo density profile in a way that accounts for the main effects of baryonic feedback in the non-linear matter power spectrum (Mead et al. 2015).

The impact of these systematic uncertainties are included in the COSMOMC (Lewis & Bridle 2002) fitting pipeline used in Hildebrandt et al. (2017), first presented in Joudaki et al. (2017). Fiducially, we use the same priors on the parameters $A_{\rm IA}$, $\eta_{\rm IA}$ and B as in Hildebrandt et al. (2017), listed in Table 1. We do not include additional

degrees of freedom in our analyses for the additive and multiplicative shear calibration corrections (Fenech-Conti et al. 2017), but incorporate these directly in our data (Hildebrandt et al. 2017). Our setup agrees with the fiducial setup of systematic uncertainties in Hildebrandt et al. (2017), given by the 'KiDS-450' row in their table 4.

Our parameter priors are identical to the priors given in Hildebrandt et al. (2017), with the exception of the baryon density and Hubble constant. We impose the conservative prior $0.013 < \Omega_b h^2 < 0.033$ on the baryon density [motivated by the big bang nucleosynthesis (BBN) constraints in Burles, Nollett & Turner 2001; Olive & Particle Data Group 2014; Cyburt et al. 2016 and $0.4 < h < 1.0$ on the dimensionless Hubble constant (which is a derived parameter). These choices can be contrasted with the tighter $0.019 < \Omega_b h^2 < 0.026$ and $0.64 < h < 0.82$ priors in Hildebrandt et al. (2017). The uniform Hubble constant prior in Hildebrandt et al. (2017) encapsulates the $\pm 5\sigma$ range from the direct measurement of Riess et al. (2016), where $h = 0.732 \pm 0.017$, and extends beyond the *Planck* CMB constraint on this parameter (Planck Collaboration XIII 2016b, where $h = 0.673 \pm 0.010$ for TT+lowP). Our prior choices are more conservative than in Hildebrandt et al. (2017) because they may otherwise have a significant impact on the extended cosmology constraints (unlike e.g. S_8 in ΛCDM that is robust to both choices of priors). However, we do consider specific cases where the Riess et al. (2016) prior on the Hubble constant is employed (e.g. see the dark energy results in Table 2).

In addition to examining extensions to the standard cosmological model with the KiDS-450 data set, and assessing their significance from a model selection standpoint, we consider the impact of these extensions on the discordance between KiDS and *Planck* (reported in Hildebrandt et al. 2017). To this end, the *Planck* measurements (Planck Collaboration XI 2016a,b) that we use are the CMB temperature and polarization on large angular scales, limited to multipoles $\ell \leq 29$ (i.e. low-ℓ TEB likelihood), and the CMB temperature on smaller angular scales (via the PLIK TT likelihood). Thus, we conservatively do not consider *Planck* polarization measurements on smaller angular scales (which would increase the discordance with KiDS slightly), and we also do not consider *Planck* CMB lensing measurements (which would decrease the discordance with KiDS slightly).

2.2 Model selection and data set concordance

As we consider extensions to the standard cosmological model, we mainly aim to address two questions. The first question pertains to model selection, i.e. whether the extended model is favoured as compared to ΛCDM. To aid in this aim, we follow Joudaki et al. (2017) in using the DIC (Spiegelhalter, Best & Carlin 2002, also see Kunz, Trotta & Parkinson 2006; Liddle 2007; Trotta 2008, and Spiegelhalter et al. 2014), given by the sum of two terms:

$$\mathrm{DIC} \equiv \chi^2_{\mathrm{eff}}(\hat{\theta}) + 2p_{\mathrm{D}}. \tag{1}$$

Here, the first term consists of the best-fitting effective $\chi^2_{\mathrm{eff}}(\hat{\theta}) = -2\ln\mathcal{L}_{\mathrm{max}}$, where $\mathcal{L}_{\mathrm{max}}$ is the maximum likelihood of the data given the model, and $\hat{\theta}$ is the vector of varied parameters at the maximum likelihood point. The second term is the 'Bayesian complexity,' $p_{\mathrm{D}} = \overline{\chi^2_{\mathrm{eff}}(\theta)} - \chi^2_{\mathrm{eff}}(\hat{\theta})$, where the bar denotes the mean over the posterior distribution. Thus, the DIC is composed of the sum of the goodness of fit of a given model and its Bayesian complexity, which is a measure of the effective number of parameters, and acts to penalize more complex models. For reference, a difference in χ^2_{eff} of 10 between two models corresponds to a probability ratio of 1 in 148, and we therefore take a positive difference in DIC of 10 to correspond to strong preference in favour of the reference model (ΛCDM), while an equally negative DIC difference corresponds to strong preference in favour of the extended model. We take $\Delta\mathrm{DIC} = 5$ to constitute moderate preference in favour of the model with the lower DIC estimate, while differences close to zero do not particularly favour one model over the other.

In Hildebrandt et al. (2017), we found that the cosmological constraints from the KiDS-450 data set are overall internally consistent, i.e. the constraints agree despite a range of changes to the treatment of the systematic uncertainties (e.g. see Fig. 10 therein). The cosmological constraints from KiDS also agree with previous lensing analyses from CFHTLenS (see Joudaki et al. 2017 and references therein) and the DES (The Dark Energy Survey Collaborations 2016), along with pre-*Planck* CMB measurements from WMAP9, ACT and SPT (Calabrese et al. 2013). However, KiDS does disagree with *Planck* (Planck Collaboration XIII 2016b) at the 2σ level in $S_8 = \sigma_8\sqrt{\Omega_{\mathrm{m}}/0.3}$, and this tension can seemingly not be resolved by the systematic uncertainties (Hildebrandt et al. 2017).

The second question that we aim to address therefore pertains to whether an extension to the fiducial treatment of the lensing systematic uncertainties or the standard cosmological model can alleviate or completely remove the tension between KiDS and *Planck*. Since current lensing data mainly constrain the S_8 parameter combination well, we quantify the tension T in this parameter, via

$$T(S_8) = \left|\overline{S_8^{D_1}} - \overline{S_8^{D_2}}\right| \Big/ \sqrt{\sigma^2\left(S_8^{D_1}\right) + \sigma^2\left(S_8^{D_2}\right)}, \tag{2}$$

where the data sets D_1 and D_2 refer to KiDS and Planck, respectively, the vertical bars extract the absolute value of the encased terms, the horizontal bars again denote the mean over the posterior distribution and σ refers to the symmetric 68 per cent confidence interval about the mean.

Moreover, to better capture the overall level of concordance or discordance between the two data sets, we calculate a diagnostic grounded in the DIC (Joudaki et al. 2017):

$$\mathcal{I}(D_1, D_2) \equiv \exp\{-\mathcal{G}(D_1, D_2)/2\}, \tag{3}$$

such that

$$\mathcal{G}(D_1, D_2) = \mathrm{DIC}(D_1 \cup D_2) - \mathrm{DIC}(D_1) - \mathrm{DIC}(D_2), \tag{4}$$

where $\mathrm{DIC}(D_1 \cup D_2)$ is obtained from the combined analysis of the data sets. Thus, $\log\mathcal{I}$ is positive when two data sets are in concordance, and negative when the data sets are discordant, with values following Jeffreys' scale (Jeffreys 1961, Kass & Raftery 1995), so that $\log\mathcal{I}$ in excess of $\pm 1/2$ is considered 'substantial', in excess of ± 1 is considered 'strong', and in excess of ± 2 is considered 'decisive' (corresponding to a probability ratio in excess of 100). In Joudaki et al. (2017), this concordance test was found to largely agree with the analogous diagnostic based on the Bayesian evidence (e.g. Marshall, Rajguru & Slosar 2006; Raveri 2016), and enjoys the benefit of being more readily obtained from existing MCMC chains. Our particular approach for propagating photometric redshift uncertainties into the analysis moreover makes the calculation of the evidence non-trivial.

2.3 Baseline settings

Our cosmology analysis is enabled by a series of MCMC runs, using the COSMOMC package (Lewis & Bridle 2002) with the lensing module presented in Joudaki et al. (2017).

In our MCMC runs, we always vary the 'vanilla' parameters $\{\Omega_c h^2, \Omega_b h^2, \theta_{MC}, n_s, \ln(10^{10} A_s)\}$, corresponding to the cold dark matter density, baryon density, approximation to the angular size of the sound horizon, scalar spectral index and amplitude of the scalar spectrum, respectively, along with the optical depth to reionization, τ, when including CMB measurements. The parameters A_s and n_s are defined at the pivot wavenumber k_{pivot}. Moreover, we always vary the baryon feedback and intrinsic alignment amplitudes, B and A_{IA} respectively, while the parameter governing the redshift dependence of the intrinsic alignment signal η_{IA} is varied in our 'extended systematics' scenario. Our treatment of the photometric redshift uncertainties does not involve any additional degrees of freedom.

We fiducially assume a flat universe and no running of the spectral index. Our fiducial cosmological model includes three massless neutrinos (adequate at the level of our constraints, negligible difference compared to assuming the 0.06 eV minimal mass of the normal hierarchy), so that the effective number of neutrinos $N_{eff} = 3.046$. We determine the primordial helium abundance as a function of N_{eff} and $\Omega_b h^2$ in a manner consistent with BBN (see e.g. equation 1 in Joudaki 2013). The Hubble constant, H_0 (expressed as h in its dimensionless form), and rms of the present linear matter density field on $8\,h^{-1}$ Mpc scales, σ_8, can be derived from the vanilla parameters. The uniform priors on the vanilla and lensing systematic parameters are listed in Table 1, which also contains the priors on the extended cosmology parameters discussed in Sections 3.2–3.8.

As part of our MCMC computations, we use the Gelman & Rubin (1992) R statistic to determine the convergence of our chains, where R is defined as the variance of chain means divided by the mean of chain variances. We enforce the conservative limit $(R-1) < 2 \times 10^{-2}$, and stop the MCMC runs after further explorations of the distribution tails.

3 RESULTS

We now investigate the KiDS-450 extended systematics and cosmology constraints. In addition to a more conservative treatment of the intrinsic galaxy alignments, baryon feedback, the cosmological extensions considered are the sum of active neutrino masses, spatial curvature, evolving dark energy (both in the form of a constant equation of state and in the form of a time-dependent parametrization), evolving dark energy with curvature, MG and running of the scalar spectral index.

The relative impact of these extensions on the lensing observables is shown in Fig. 1. We consider the relative preference of these extended models as compared to the standard model in Table 2, and the impact of the extensions on the relative concordance between KiDS and *Planck* in Table 3. We only determine the joint KiDS+*Planck* parameter constraints in the event the two data sets are not in tension. Our criterion for this is $\log \mathcal{I} > 0$.

3.1 ΛCDM (extended lensing systematics)

In Hildebrandt et al. (2017), we employed informative priors on the Hubble constant and baryon density ($\pm 5\sigma$ of the constraints in Riess et al. 2016 and Cyburt et al. 2016, respectively), but here we consider less informative priors on these parameters, in accordance with Table 1, as we move away from the fiducial ΛCDM model.

In Fig. 2, we show the cosmological constraints from KiDS in the σ_8–Ω_m plane, both using the same parameter priors as in Hildebrandt et al. (2017), and then widening the priors on the Hubble constant and baryon density in accordance with Table 1. As previously noted in Joudaki et al. (2017) and Hildebrandt et al. (2017), wider priors mainly extend the lensing contours along the degeneracy direction, and do not remove the tension with *Planck*. Thus, for both choices of priors, the tension between KiDS weak lensing and *Planck* CMB temperature (TT+lowP) measurements is approximately 2σ, when quantified via the $S_8 = \sigma_8(\Omega_m/0.3)^{0.5}$ parameter combination that lensing measures well. Accounting for the full parameter space, we find $\log \mathcal{I} = -0.63$ (defined in Section 2.2, and shown in Table 3), which corresponds to 'substantial discordance' between the KiDS and *Planck* data sets. This is similar to the value $\log \mathcal{I} = -0.79$ found in Hildebrandt et al. (2017), despite the different priors on the Hubble constant and baryon density.

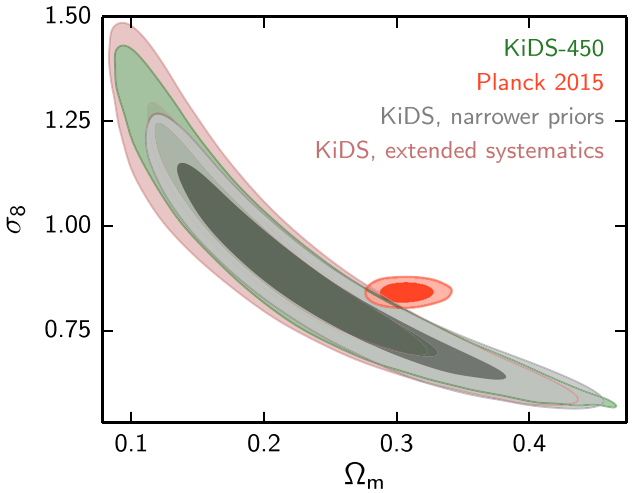

Figure 2. Marginalized posterior contours in the σ_8–Ω_m plane (inner 68% CL, outer 95% CL). We show our fiducial KiDS constraints in green, KiDS with narrower priors on the Hubble constant and baryon density in grey (as in Hildebrandt et al. 2017), KiDS with extended treatment of the astrophysical systematics in pink, and *Planck* in red.

We also examine the robustness of our fiducial treatment of the systematic uncertainties in KiDS, by allowing for a possible redshift dependence of the intrinsic alignment signal (via η_{IA}), and simultaneously widening the priors on the intrinsic alignment amplitude, A_{IA}, and baryon feedback amplitude B entering HMCODE. Extending the prior on B allows us to consider a greater range of feedback models. As some of the feedback models considered in the latest OWL simulations (cosmo-OWLS; Le Brun et al. 2014) are more extreme in the violence they inflict on the matter power spectrum than those in the original OWLS models (Schaye et al. 2010; van Daalen et al. 2011), extending to low values of B is an attempt to encompass this greater range of behaviours.

We follow the strategy adopted in Hildebrandt et al. (2017) to account for uncertainties in the multiplicative shear calibration correction and in the source redshift distributions. The analysis of Fenech-Conti et al. (2017) showed that the shear calibration for KiDS is accurate at the level of $\lesssim 1$ per cent, an error that is propagated by modifying the data covariance matrix (see equation 12 in Hildebrandt et al. 2017). We used a range of different methods in Hildebrandt et al. (2017) to validate the 'DIR' calibrated redshift distributions that we adopt, and use bootstrap realizations of the set of tomographic redshift distributions to propagate our uncertainty on this redshift measurement through to cosmological parameter constraints (further see section 6.3 of Hildebrandt et al. 2017). We note that the accuracy of this redshift calibration method will

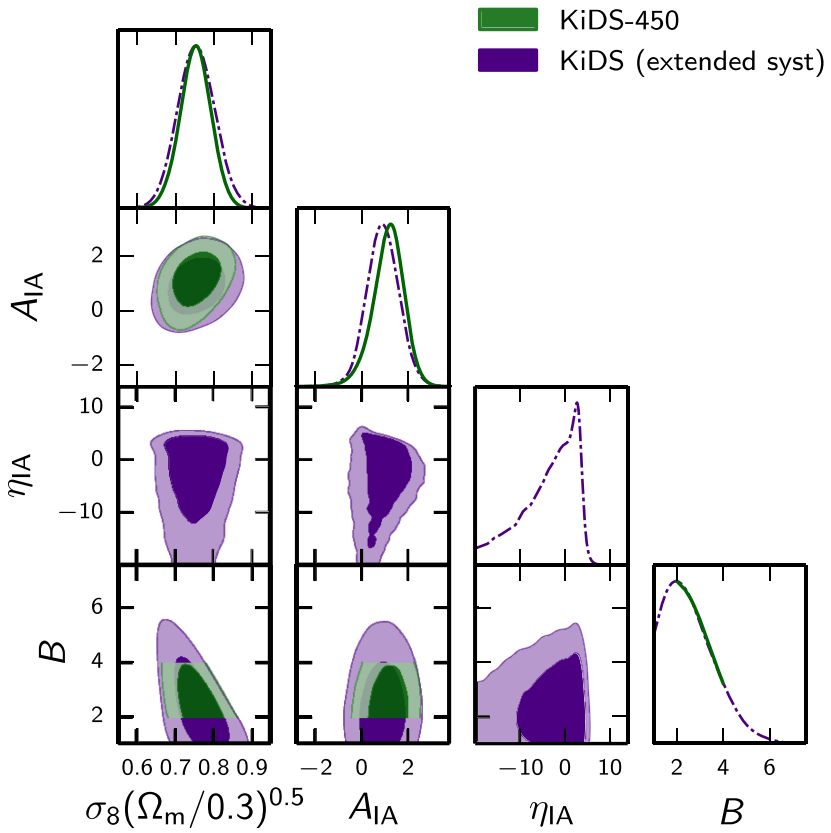

Figure 3. Marginalized posterior distributions of the lensing systematics parameters and their correlation. The vanilla parameters are simultaneously included in the analysis. We show KiDS with the fiducial treatment of systematic uncertainties in green (solid), and KiDS with the extended treatment of the lensing systematics in purple (dot–dashed). Parameter definitions and priors are listed in Table 1.

continue to improve with the acquisition of additional spectroscopic redshifts to reduce the sample variance, which we estimate to be subdominant for KiDS-450 (see appendix C3.1 in Hildebrandt et al. 2017).

We are confident that this approach correctly propagates the known measured uncertainty in the multiplicative shear calibration correction and source redshift distributions but recognize that there could always be sources of systematic uncertainty that are currently unknown to the weak lensing community. Appendix A of Hildebrandt et al. (2017) presents a Fisher matrix analysis that calculates how increasing the uncertainty on the shear calibration or redshift distribution results in an increase in the error on S_8. In our Appendix A, we verify the results of the Fisher matrix analysis by repeating our MCMC analysis allowing for an arbitrarily chosen Gaussian uncertainty of ± 10 per cent on the amplitudes of each of the tomographic shear correlation functions. The addition of these four new nuisance parameters could represent an unknown additional uncertainty in one or both of the shear and redshift calibration corrections. We find that the addition of these arbitrary nuisance parameters increases the error on S_8 by 15 per cent in agreement with the Fisher matrix analysis of Hildebrandt et al. (2017).

As shown in Fig. 1 (also see Semboloni et al. 2011; Semboloni, Hoekstra & Schaye 2013; Joudaki et al. 2017), the baryon feedback suppresses the shear correlation functions on small angular scales across all tomographic bins, with a greater amount for a given angular scale in $\xi_-^{ij}(\theta)$ than in $\xi_+^{ij}(\theta)$. The suppression is larger in $\xi_-^{ij}(\theta)$ than $\xi_+^{ij}(\theta)$ because the former is more sensitive to non-linear scales in the matter power spectrum for a given angular scale. By contrast, the intrinsic alignments mainly suppress the cross-tomographic bins, fairly uniformly across angular scale, and by approximately the same amount in $\xi_+^{ij}(\theta)$ as in $\xi_-^{ij}(\theta)$. The impact of a negative $\eta_{\rm IA}$ is to diminish the intrinsic alignment signal with increasing redshift, while a positive value boosts the intrinsic alignments with increasing redshift.

In Fig. 2, we find that the combined effect of the extensions in the lensing systematics modelling on the KiDS contour in the σ_8–$\Omega_{\rm m}$ plane is small, as the contour mildly expands in a region of high σ_8 and low $\Omega_{\rm m}$ where *Planck* is not located. The discordance between KiDS and *Planck* remains approximately the same, at the level of 1.8σ in S_8, and with $\log \mathcal{I} = -0.70$. The slight decrease in the S_8 tension is not due to a noticeable shift in the KiDS estimate, but instead due to a 25 per cent increase in the uncertainty of the marginalized S_8 constraint (which picks up contributions from the widened contour in the full σ_8–$\Omega_{\rm m}$ plane, even away from the *Planck* contour).

In Fig. 3, we show a triangle plot of the constraints in the subspace of the extended systematics parameters ($A_{\rm IA}$, $\eta_{\rm IA}$, B) along with S_8. We constrain the baryon feedback amplitude $B < 4.6$ (or $\log B < 0.66$) at 95% confidence level (CL), with a peak around $B = 2$, which most closely corresponds to the 'AGN' case in Mead et al. (2015). We constrain the intrinsic alignment redshift dependence to be consistent with zero, where $-16 < \eta_{\rm IA} < 4.7$ (95% CL). Although the posterior peaks for $\eta_{\rm IA} \gtrsim 0$, it has a sharp cutoff in the positive domain (as it boosts the IA signal and decreases the

total lensing signal) and a long tail in the negative domain (as it diminishes the IA signal and does not contribute to the total lensing signal).

Despite the redshift dependent degree of freedom, we continue to find an almost 2σ preference for a non-zero intrinsic alignment amplitude, where $-0.45 < A_{\rm IA} < 2.3$, which is similar to our constraint of $-0.24 < A_{\rm IA} < 2.5$ when considering the fiducial treatment of the systematic uncertainties. Both of these constraints are included in Fig. 4, which shows that the IA amplitude posteriors are remarkably consistent regardless of the systematic uncertainties and underlying cosmological model (discussed in forthcoming sections). Given the different imprints on the lensing observables, we find no significant correlation between the intrinsic alignment and baryon feedback parameters in Fig. 3. However, we do find a weak correlation between S_8 and the feedback amplitude.

In Table 2, we show that although the extended systematics model improves the fit to the KiDS measurements by $\Delta\chi^2 = -2.1$ as compared to the fiducial model, it is marginally disfavoured by $\Delta{\rm DIC} = 2.4$. Thus, in addition to not noticeably improving the discordance with *Planck*, extending the treatment of the systematic uncertainties in KiDS is marginally disfavoured as compared to the fiducial treatment of the systematic uncertainties. We therefore also consider a 'large-scale' cut, where we follow the approach in Planck Collaboration XIV (2016c) by removing all angular bins in the KiDS measurements except for the two bins centred at $\theta = \{24.9, 50.7\}$ arcmin in $\xi_+^{ij}(\theta)$, and the one bin centred at $\theta = 210$ arcmin in $\xi_-^{ij}(\theta)$. The downsized data vector consists of 30 elements (from the fiducial 130 elements), and the angular scales that are kept are effectively insensitive to any non-linear physics in the matter power spectrum, as for example seen for the case of baryons in Fig. 1. However, the substantial discordance with *Planck* persists despite the removal of small scales in the lensing measurements, where $\log\mathcal{I} = -0.62$ and $T(S_8) = 1.9\sigma$ (as $S_8 = 0.55^{+0.32}_{-0.29}$ at 95% CL decreases away from *Planck* but has larger uncertainty).

In addition to changes in the treatment of the weak lensing systematic uncertainties and removal of small angular scales in the KiDS measurements, the tension with *Planck* is also robust to changes in the choice of the CMB measurements. Including small-scale polarization information (*Planck* TT, TE, EE+lowP) increases the tension by another 0.2σ, while including CMB lensing measurements (*Planck* TT+lowP+lensing) decreases the tension by roughly the same amount. Given our inability to resolve the discordance between KiDS and *Planck* in the context of the standard ΛCDM model, we therefore proceed by turning our attention to extensions to the underlying cosmological model (with fiducial treatment of the systematic uncertainties), and examine to what extent these cosmological models are favoured by the data while simultaneously alleviating the discordance between the two data sets.

3.2 Neutrino mass

As we explore extensions to the standard model of cosmology, we begin by allowing for the sum of neutrino masses to vary as a free parameter in our MCMC analysis. Since massive neutrinos suppress the clustering of matter below the neutrino free-streaming scale, we need to adequately account for this in our estimation of the matter power spectrum over a range of redshifts and scales.

To this end, we use the updated Mead et al. (2016) version of HMCODE which can account for the impact of massive neutrinos on the non-linear matter power spectrum in tandem with other physical effects, such as baryonic feedback. HMCODE is a tweaked version of

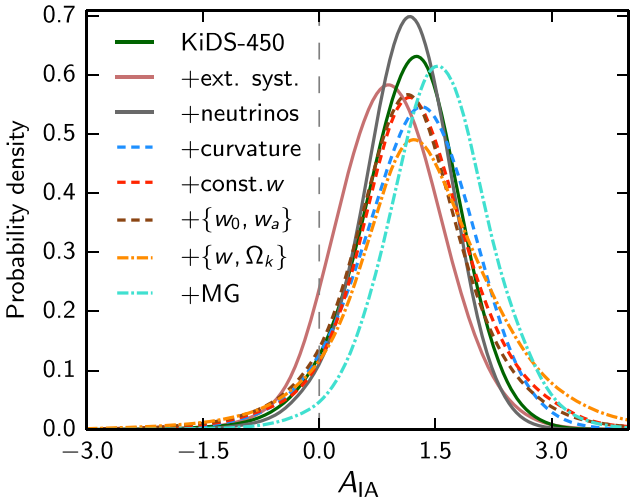

Figure 4. Marginalized posterior distributions for the intrinsic alignment amplitude considering different extended models.

the halo model, and as such the non-linear matter power spectrum it predicts responds to new physical effects in a reasonable way, even without additional calibration. To improve an already good match to the massive neutrino simulations of Massara, Villaescusa-Navarro & Viel (2014, which assume a degenerate hierarchy with sum of neutrino masses between 0.15 and 0.60 eV), two physically motivated free parameters were introduced in Mead et al. (2016) that were then calibrated to these simulations. The updated HMCODE prescription matches the massive neutrino simulations at the few per cent level (in the tested range $z \leq 1$ and $k \leq 10\,h\,{\rm Mpc}^{-1}$), which is a minor improvement compared to the fitting formula of Bird, Viel & Haehnelt (2012), but with the additional benefit of simultaneously accounting for the impact of baryons.

In Fig. 1, we show the impact of three neutrinos with degenerate masses adding up to 1 eV on the shear correlation functions when using HMCODE for the modelling of the non-linear matter power spectrum. As expected, the neutrino masses suppress the shear correlation functions on small angular scales, at roughly the same level across tomographic bins, and at a greater level in $\xi_-^{ij}(\theta)$ as compared to $\xi_+^{ij}(\theta)$, as the former is more sensitive to non-linear scales in the matter power spectrum. In massive neutrino simulations, one finds that the matter power spectrum with massive neutrinos receives a boost beyond $k \approx 1\,h\,{\rm Mpc}^{-1}$ (e.g. see fig. 3 in Mead et al. 2016). We observe this 'spoon-like' feature in the $\xi_-^{ij}(\theta)$ ratio within the angular scales probed by KiDS, and more prominently in the small-scale region that has been masked out. This indicates that probing these small scales (and beyond) could better help to disentangle the imprints of massive neutrinos from that of baryons (also see e.g. MacCrann et al. 2017).

In Fig. 5, we show constraints in the $\sigma_8 - \Omega_{\rm m}$ and $\sum m_\nu$–$\Omega_{\rm m}$ planes. We continue to assume a degenerate neutrino mass hierarchy (adequate at the level of our constraints, also see e.g. Hall & Challinor 2012), with the sum of neutrino masses as a free parameter in addition to the standard five ΛCDM parameters and two weak lensing systematics parameters ($A_{\rm IA}$ and B, all listed in Table 1). Allowing for the neutrinos to have mass pushes both the KiDS and *Planck* contours towards larger values of $\Omega_{\rm m}$ and smaller values of σ_8, but only along the degeneracy direction. Thus, although the KiDS and *Planck* contours are in greater contact, the tension in S_8 remains high at 2.4σ. On the other hand, accounting

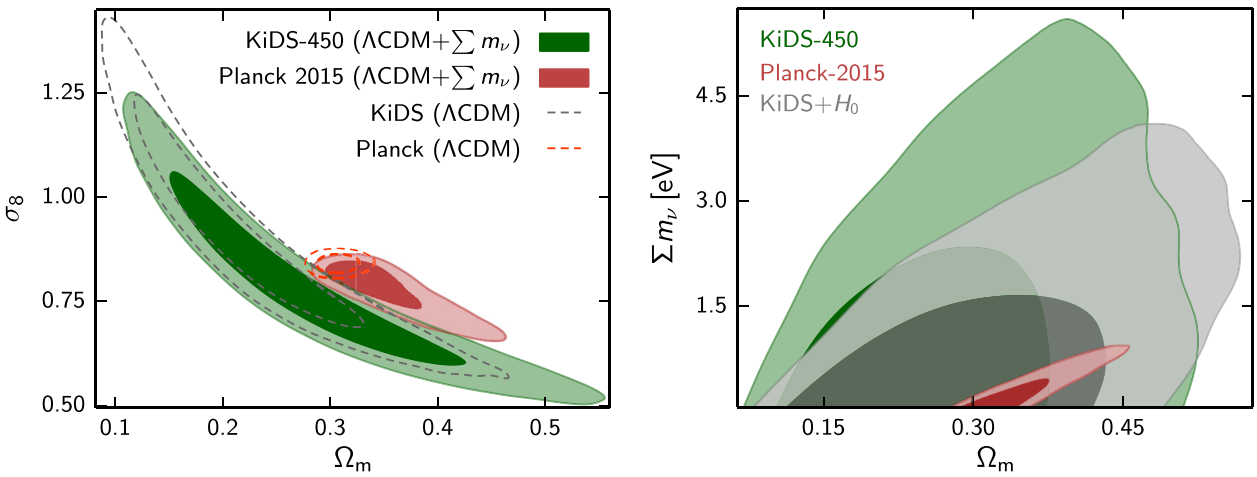

Figure 5. Left: Marginalized posterior contours in the σ_8–Ω_m plane (inner 68% CL, outer 95% CL) in a universe with massive neutrinos for KiDS in green and *Planck* in red. For comparison, dashed contours assume fiducial ΛCDM. Right: Marginalized posterior contours in the $\sum m_\nu$–Ω_m plane for KiDS in green, KiDS with informative H_0 prior in grey (from Riess et al. 2016) and *Planck* in red.

for the full parameter space, we find $\log \mathcal{I} = -0.011$, which indicates there is neither discordance nor concordance between the two data sets.

In the right-hand panel of Fig. 5, we find that the KiDS data set is not sufficiently powerful to provide a strong bound on the sum of neutrino masses, with $\sum m_\nu < 4.0$ eV at 95% CL (consistent with the power spectrum analysis in Köhlinger et al., in preparation). By imposing a uniform $\pm 5\sigma$ prior on the Hubble constant from Riess et al. (2016), the KiDS constraint improves to $\sum m_\nu < 3.0$ eV (95% CL). If one were to combine KiDS with *Planck* (given $\log \mathcal{I} \approx 0$), the addition of KiDS would only improve the *Planck* constraint on the sum of neutrino masses by 20 per cent (such that $\sum m_\nu < 0.58$ eV at 95% CL). As shown in Fig. 4, the constraint on the intrinsic alignment amplitude in this extended cosmology is only marginally affected by the inclusion of neutrino mass as a free parameter in our analysis, where $-0.12 < A_{IA} < 2.3$ (95% CL). If one were to combine KiDS with *Planck* (again as $\log \mathcal{I} \approx 0$), the constraint would improve to $0.43 < A_{IA} < 2.0$ (95% CL).

Despite alleviating the discordance with *Planck*, the neutrino mass degree of freedom is not required by the data, as the difference in DIC relative to fiducial ΛCDM is 2.7 for KiDS, 3.4 for *Planck*, and 3.3 for KiDS+*Planck*. Moreover, the KiDS constraints on the sum of neutrino masses are not competitive with that of other data combinations; for instance, *Planck* with baryon acoustic oscillation (BAO) measurements from the 6dF Galaxy Survey (Beutler et al. 2011), SDSS Main Galaxy Sample (Ross et al. 2015) and BOSS LOWZ/CMASS samples (Anderson et al. 2014) constrain $\sum m_\nu < 0.21$ eV at 95% CL (Planck Collaboration XIII 2016b).

In Fig. 6, we show our neutrino mass constraints in the plane with S_8. We consider using HMCODE with the fiducial treatment of the baryon feedback amplitude as a free parameter (i.e. corresponding to the same KiDS results in Fig. 5), and we consider using HMCODE with the feedback amplitude fixed to $B = 3.13$ (along with fixing the bloating parameter to $\eta_{\rm HMCODE} = 0.603$, in lieu of being determined by B), corresponding to a 'DM-only' scenario. While the neutrino mass constraints are not significantly affected by these two different HMCODE scenarios, the KiDS constraint on S_8 is pushed further away from *Planck* when fixing the feedback amplitude to the DM-only value.

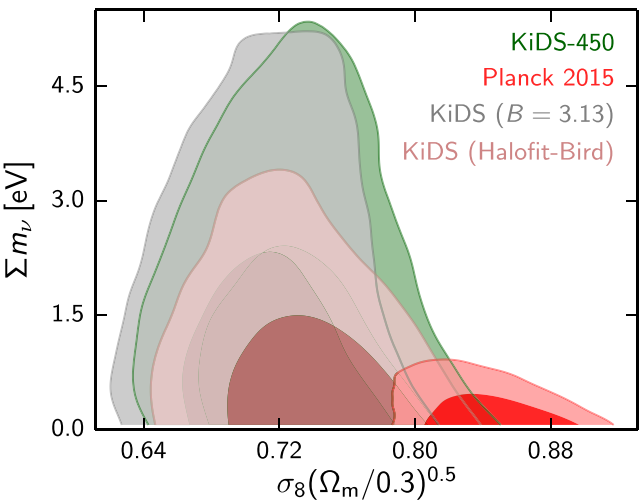

Figure 6. Marginalized posterior contours in the $\sum m_\nu$–S_8 plane (inner 68% CL, outer 95% CL). We show the results for KiDS in green with the fiducial treatment of baryons in HMCODE. We fix the feedback amplitude B in HMCODE to its DM-only value in grey, we use HALOFIT instead of HMCODE in pink, and we consider *Planck* in red.

We compare the KiDS constraints in the $\sum m_\nu$–S_8 plane to the case where the HALOFIT prescription (Bird et al. 2012; Takahashi et al. 2012) is used to model the non-linear matter power spectrum. Although HALOFIT, which is unable to account for the effect of baryonic physics in the non-linear matter power spectrum, agrees well with HMCODE with DM-only settings, the KiDS neutrino mass bound with HALOFIT is stronger at $\sum m_\nu < 2.5$ eV (95% CL). Moreover, the KiDS contour with HALOFIT is less in tension with *Planck* than when using HMCODE with DM-only settings, at a level of 2.5σ with HALOFIT as compared to 3.0σ with HMCODE. These differences in both neutrino mass constraint and discordance with *Planck* illustrate the importance of an accurate prescription for the modelling of the non-linear matter power spectrum (also see Natarajan et al. 2014).

In Fig. 7, we show how the *Planck* measurement of the Hubble constant changes as a function of the underlying cosmology. It is

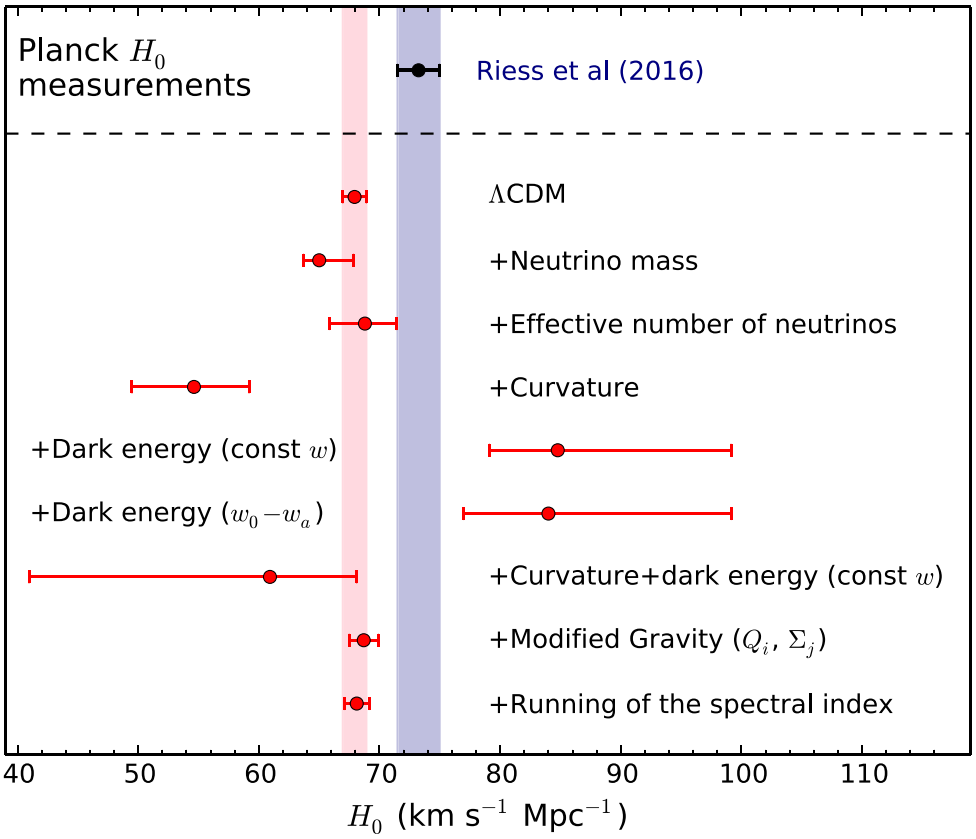

Figure 7. Hubble constant constraints at 68% CL in our fiducial and extended cosmologies, for *Planck* in red (Planck Collaboration XIII 2016b) as compared to the direct measurement of Riess et al. (2016) in purple. We do not show the corresponding constraints for KiDS, as it is unable to measure the Hubble constant. Our ΛCDM constraint on the Hubble constant ($h = 0.679 \pm 0.010$) differs marginally from that in Planck Collaboration XIII (2016b, $h = 0.673 \pm 0.010$) due to different priors, in particular our fiducial model fixes the neutrinos to be massless.

well known that the CMB temperature constraint on the Hubble constant is anticorrelated with the sum of neutrino masses (e.g. Joudaki 2013; Planck Collaboration XIII 2016b). The *Planck* measurement of the Hubble constant in a cosmology with $\sum m_\nu$ as a free parameter therefore shifts it further away from local measurements of H_0. The discordance between the *Planck* (TT+lowP) measurement of the Hubble constant ($h = 0.673 \pm 0.010$) and the local measurement in Riess et al. (2016, $h = 0.732 \pm 0.017$) is 2.7σ in our fiducial ΛCDM cosmology with massless neutrinos. In a cosmology with $\sum m_\nu$ as a free parameter, this discordance increases with $0.599 < h < 0.689$ at 95% CL.

While the KiDS data set is not particularly sensitive to the effective number of neutrinos $N_{\rm eff}$, we note that this additional degree of freedom does help to bring the *Planck* constraint on the Hubble constant in agreement with the direct measurement of Riess et al. (2016). This is mainly achieved by widening the *Planck* error bars on the Hubble constant, such that $0.635 < h < 0.746$ (95% CL), with $N_{\rm eff} = 3.15 \pm 0.32$. However, *Planck* does not favour this additional degree of freedom, as $\Delta{\rm DIC} = 1.1$.

3.3 Curvature

We now move to constraining deviations from spatial flatness and examine the model selection and data set concordance outcomes of this new degree of freedom for KiDS and *Planck*.

In Fig. 1, we show that a negative curvature (corresponding to a positive Ω_k) decreases the shear signal, fairly uniformly across $\xi_\pm^{ij}(\theta)$ over the angular scales probed by KiDS, such that its signature can in principle be disentangled from that of lensing systematics such as baryons and intrinsic alignments. We note that when Ω_k is varied, H_0 is also varying to keep $\theta_{\rm MC}$ fixed (as the former is a derived parameter, while the latter is a primary parameter). If we vary the curvature by the same amount, and simultaneously vary $\theta_{\rm MC}$ such that H_0 is kept fixed instead, the decrease in the shear correlation functions reduces by almost an order of magnitude. Meanwhile, CMB temperature measurements of the curvature are highly correlated with the Hubble constant and matter density (due to their degeneracy in the angular diameter distance to the last scattering surface). The *Planck* constraint on the curvature mainly originates from the signatures of lensing in the CMB temperature power spectrum, the late-time integrated Sachs–Wolfe effect, and the lower boundary of the H_0 prior (e.g. Komatsu et al. 2009; Planck Collaboration XIII 2016b).

As a result, given that we exclude CMB lensing ($\phi\phi$), *Planck* is no longer able to constrain the matter density well when allowing Ω_k to vary, causing a nearly horizontal elongation of the *Planck* contour towards larger values of the matter density in the σ_8–$\Omega_{\rm m}$ plane of Fig. 8 (and thereby larger S_8), while KiDS largely moves along the degeneracy direction towards smaller values of the matter density (with a minor offset that decreases S_8). The overall effect of these changes is to increase the tension between KiDS and *Planck* to 3.5σ in S_8 (where the main cause of the increased tension is the new *Planck* constraint, which has shifted by a factor of six of the original uncertainty in S_8). Although *Planck* constrains S_8 more strongly than KiDS in a flat ΛCDM universe (by a factor of 1.7), the KiDS constraint on S_8 is a factor

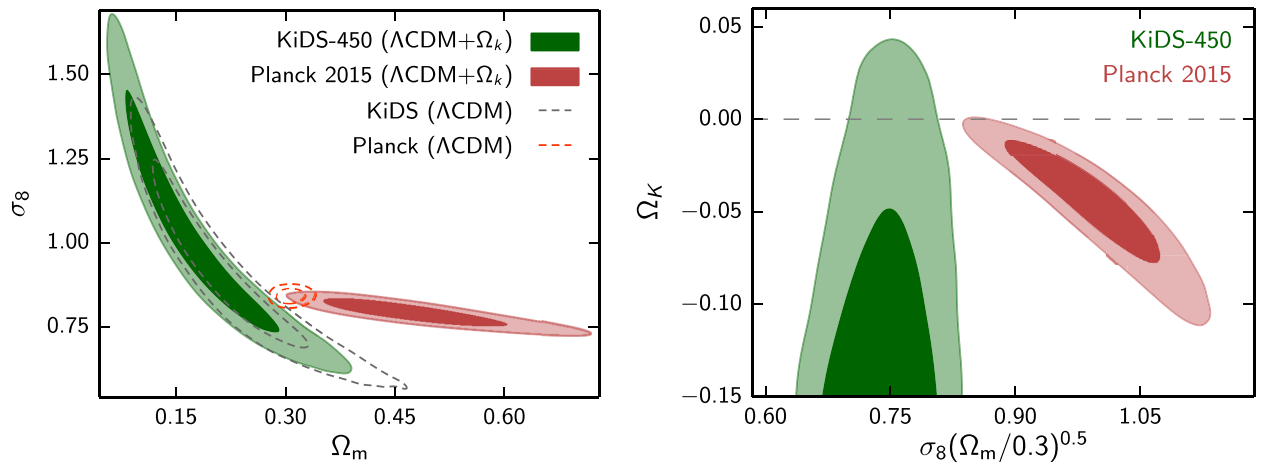

Figure 8. Left: Marginalized posterior contours in the σ_8–Ω_m plane (inner 68% CL, outer 95% CL) in a universe with non-zero curvature for KiDS in green and *Planck* in red. For comparison, dashed contours assume fiducial ΛCDM. Right: Marginalized posterior contours in the Ω_k–S_8 plane for KiDS in green and *Planck* in red. The dashed horizontal line denotes flatness.

of 1.6 stronger than the constraint from *Planck* when Ω_k is allowed to vary.

Accounting for the full parameter space, $\log \mathcal{I} = -1.7$, which corresponds to 'strong discordance' between the KiDS and *Planck* data sets. In the Ω_k–S_8 plane of Fig. 8, the KiDS and *Planck* contours prefer $\Omega_k < 0$, both at approximately 95% CL. Despite the deviation from flatness, the KiDS intrinsic alignment amplitude remains robustly determined as shown in Fig. 4, marginally widening to $-0.38 < A_{IA} < 2.8$ (95% CL). While *Planck* weakly-to-moderately favours non-zero curvature with $\Delta\text{DIC} = -4.3$ (down from $\Delta\chi^2_{\text{eff}} = -5.8$ due to the increased Bayesian complexity), the additional degree of freedom is not favoured by KiDS, with $\Delta\text{DIC} \simeq 0$. Moreover, as shown in Fig. 7, the *Planck* constraint on the Hubble constant ($0.46 < h < 0.65$ at 95% CL) moves it further away from the Riess et al. (2016) result. Although the combination of weak lensing and CMB can significantly improve the constraint on the curvature (e.g. Kilbinger et al. 2013; Planck Collaboration XIII 2016b), we do not provide joint KiDS+*Planck* constraints on Ω_k as the two data sets are discordant in this extended cosmology.

3.4 Dark energy (constant w)

We now turn away from the assumption of a cosmological constant by considering evolving dark energy. We begin by allowing for a constant dark energy equation of state w that can vary freely in our MCMC analyses. While we have discussed HMCODE's ability to account for the impact of baryons and massive neutrinos in the non-linear matter power spectrum, HMCODE's calibration to the Coyote N-body simulations also included models with $-0.7 < w < 1.3$ (Mead et al. 2015). Our prior on w extends beyond this range, but we expect our results to be only marginally biased, as the cosmological constraints are either too weak or tend to lie near $w = -1$. Moreover, in contrast to e.g. a fitting function, the physical grounding of HMCODE in the halo model allows one to probe fairly extreme values of w and still trust the modelling, as changes to the underlying cosmology diffuse through into the matter power spectrum prediction in a natural way (via the mass–concentration relation and evolution of the halo mass function).

In Fig. 1, we show the imprint of a constant dark energy equation of state on the shear correlation functions, while keeping all primary parameters fixed. An increase in the equation of state, such that $w > -1$, causes a scale-dependent suppression in the matter power spectrum relative to a cosmological constant (e.g. Joudaki & Kaplinghat 2012; Mead et al. 2016). For a fixed Hubble constant, $w > -1$ also suppresses the lensing kernel relative to a cosmological constant (as it boosts $H(z)/H_0$), but this is not the case in Fig. 1 as θ_{MC} is kept fixed in lieu of the Hubble constant which varies from one cosmology to another (since θ_{MC} is a primary parameter while H_0 is treated as a derived parameter). Thus, when fixing our primary parameters, the lensing kernel increases for $w > -1$, partly cancelling the suppression in the matter power spectrum.

In Fig. 9, we show the constraints in the σ_8–Ω_m and w–S_8 planes when allowing for $w \neq -1$. The KiDS and *Planck* contours now overlap in the σ_8–Ω_m plane, both due to a fairly uniform increase in the area of the KiDS contour perpendicular to the lensing degeneracy direction (noting that the lensing constraints parallel to the degeneracy direction are prior dependent), and due to a shift in the *Planck* contour perpendicular to the lensing degeneracy direction. The realignment of the CMB contour along the lensing degeneracy direction was also found for CFHTLenS and *WMAP7* in Kilbinger et al. (2013), and the extension of the *Planck* contour along the Ω_m axis is due to the same geometric degeneracy as in the case of a non-zero curvature. As a result, the respective KiDS and *Planck* S_8 constraints agree at 1σ (despite seemingly being in tension in the w–S_8 plane). Accounting for the full parameter space, we find $\log \mathcal{I} = 0.99$, which effectively corresponds to 'strong concordance' between the KiDS and *Planck* data sets. In addition to removing the tension between these data sets, the *Planck* constraint on the Hubble constant is now also wider than in ΛCDM ($0.66 < h < 1.0$ at 95% CL, where the upper bound is hitting against the prior) and in agreement with the Riess et al. (2016) direct measurement of H_0.

In the w–S_8 plane, KiDS and *Planck* are both in agreement with a cosmological constant, while the combined analysis of KiDS+*Planck* seems to favour a 2.6σ deviation from ΛCDM (marginalized constraint of $-1.93 < w < -1.06$ at 99% CL). As noted in Planck Collaboration XIII (2016b), deviations from a cosmological constant seem to be preferred by large values of the Hubble constant (that are arguably ruled out), and so we also consider a $\pm 5\sigma$ uniform Riess et al. (2016) prior on H_0. While the KiDS+*Planck*+H_0 contour tightens and moves towards $w = -1$, we still find an approximately 2σ deviation from a cosmological

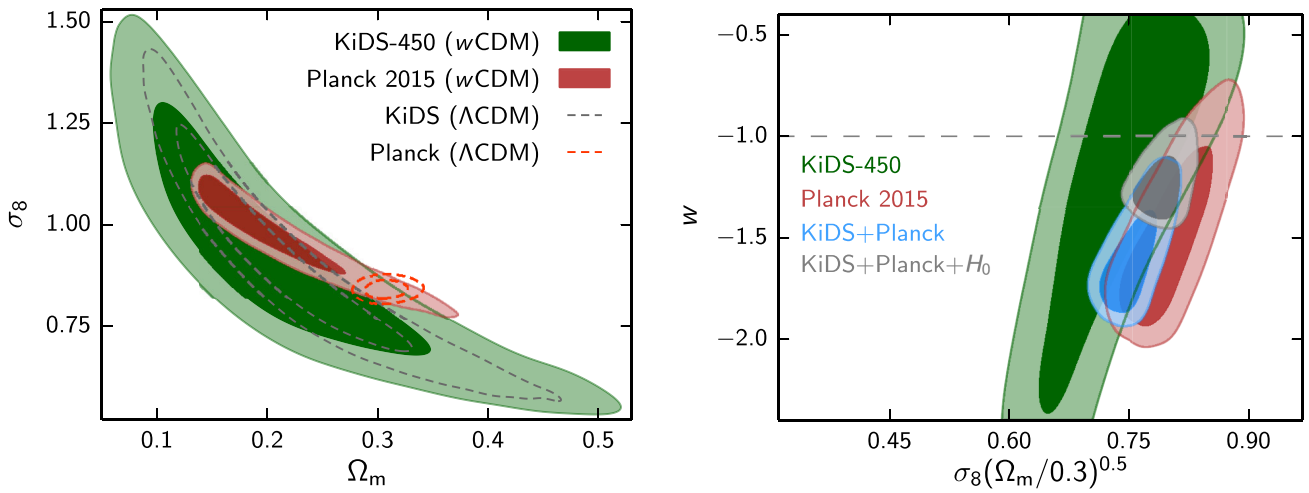

Figure 9. Left: Marginalized posterior contours in the σ_8–Ω_m plane (inner 68% CL, outer 95% CL) in a universe with a constant dark energy equation of state for KiDS in green and *Planck* in red. For comparison, dashed contours assume fiducial ΛCDM. Right: Marginalized posterior contours in the w–S_8 plane for KiDS in green, *Planck* in red, KiDS+*Planck* in blue and KiDS+*Planck* with informative H_0 prior in grey (from Riess et al. 2016). The dashed horizontal line denotes the ΛCDM prediction.

constant (marginalized constraint of $-1.42 < w < -1.01$ at 95% CL). As in other extended cosmologies, the intrinsic alignment amplitude remains robustly determined when allowing w to vary, with 95% CLs at $-0.50 < A_{IA} < 2.9$ for KiDS, $0.27 < A_{IA} < 3.0$ for KiDS+*Planck* and $0.38 < A_{IA} < 2.4$ for KiDS+*Planck*+H_0.

We have shown that the introduction of a constant dark energy equation of state seems to remove the discordance between KiDS and *Planck*, and between local Hubble constant measurements and *Planck*, while moreover deviating from a cosmological constant when these measurements are combined. However, we also want to know to what extent the constant w model is favoured or disfavoured by the data. We find that KiDS and *Planck* on their own show no preference for $w \neq -1$, with $\Delta\text{DIC} = 2.3$ for KiDS and $\Delta\text{DIC} = -0.20$ for *Planck* (respectively degraded from $\Delta\chi^2_{\rm eff} = 0.074$ and $\Delta\chi^2_{\rm eff} = -3.1$ due to the increased Bayesian complexity). However, the combination of KiDS+*Planck* seems to prefer the constant dark energy equation of state model with $\Delta\text{DIC} = -5.4$ (with near identical Bayesian complexity to ΛCDM), while this preference reduces to $\Delta\text{DIC} = -2.9$ when further considering KiDS+*Planck*+H_0 (marginally degraded from $\Delta\chi^2_{\rm eff} = -3.4$). Thus, from the point of model selection, we only find weak preference in favour of a constant dark energy equation of state model as compared to standard ΛCDM.

3.5 Dark energy ($w_0 - w_a$)

Although a constant dark energy equation of state as a free parameter constitutes the simplest deviation from a $w = -1$ model, there is no strong theoretical motivation to keep the equation of state constant once one has moved away from the cosmological constant scenario. We therefore also consider a time-dependent parametrization to the equation of state, in the form of a first-order Taylor expansion with two free parameters:

$$w(a) = w_0 + (1 - a)w_a, \tag{5}$$

where a is the cosmic scalefactor, w_0 is the dark energy equation of state at present and $w_a = -\mathrm{d}w/\mathrm{d}a|_{a=1}$ (which can also be expressed as $w_a = -2\mathrm{d}w/\mathrm{d}\ln a|_{a=1/2}$; Chevallier & Polarski 2001; Linder 2003).

In Fig. 1, we show the impact of a time dependence of the equation of state on the shear correlation functions. Since a negative w_a makes the overall equation of state more negative with time, it has the opposite impact on the matter power spectrum and lensing kernel (and thereby shear correlation functions) to the case where $w > -1$ discussed in Section 3.4. Clearly the benefit of two degrees of freedom to describe the dark energy is that more complex behaviour of the shear correlation functions is allowed than when only a constant equation of state is considered, enhancing the ability of the theoretical model to describe the data. Meanwhile, the extra degree of freedom from non-zero w_a further adds to the geometric degeneracy of the CMB measurements.

Along with the case where the dark energy equation of state is constant, HMCODE accurately accounts for the impact of $w_0 - w_a$ models on the non-linear matter power spectrum, as demonstrated by the N-body simulations in Mead et al. (2016), covering $-1.0 < w_a < 0.75$ to $z \leq 1$ and $k \leq 10\,h\,\mathrm{Mpc}^{-1}$ (using a modified version of the GADGET-2 code of Springel 2005). HMCODE's excellent performance, which is similar to that of HALOFIT over the redshifts and scales considered, derives from the fact that the halo model is firmly grounded in physical reality. As a result, the non-linear power spectrum responds to cosmological extensions in a reasonable way via the linear growth, halo mass function, and halo mass–concentration relation, and has been shown to produce an excellent match to the non-linear response in simulations for a range of other dark energy models with a time-varying equation of state (Mead et al. 2016). For these reasons, we expect HMCODE to be adequate over our full prior range.

Using HMCODE to describe the non-linear matter power spectrum, we constrain the two degrees of freedom w_0 and w_a along with the vanilla and lensing systematics parameters (and CMB degrees of freedom when applicable). In Fig. 10, we show these constraints in the σ_8–Ω_m and w_0–w_a planes. Similar to the case where the equation of state is constant (Section 3.4), KiDS and *Planck* overlap in the σ_8–Ω_m plane, and are no longer in tension in the S_8 parameter (1σ agreement). When accounting for the full parameter space, $\log\mathcal{I} = 0.82$, which corresponds to 'substantial concordance' between the KiDS and *Planck* data sets. Moreover, as shown in Fig. 7, the *Planck* constraint on the Hubble constant is

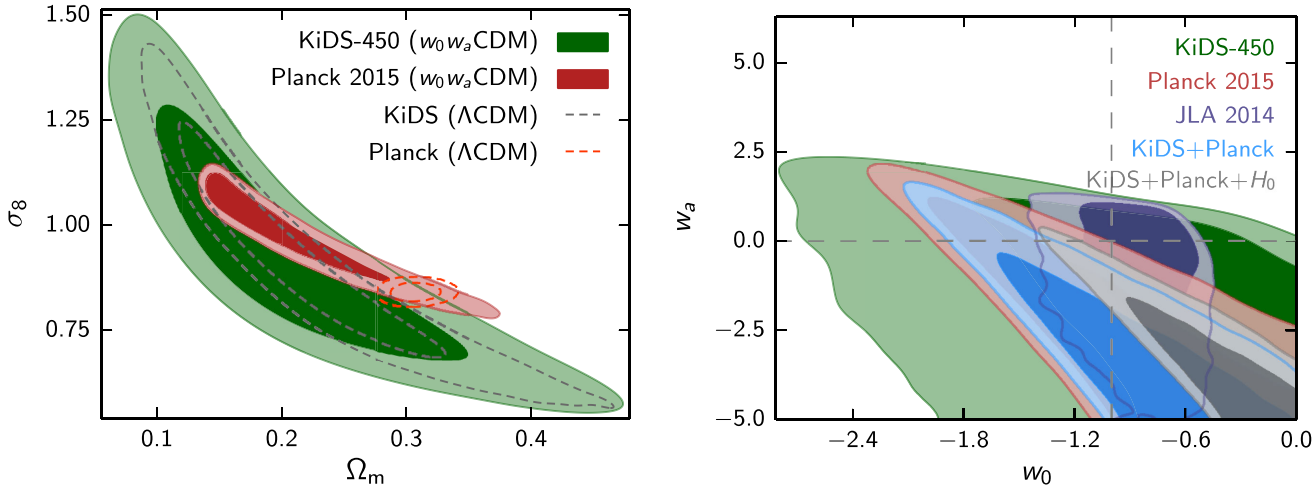

Figure 10. Left: Marginalized posterior contours in the σ_8–Ω_m plane (inner 68% CL, outer 95% CL) in a universe with a time-dependent dark energy equation of state for KiDS in green and *Planck* in red. For comparison, dashed contours assume fiducial ΛCDM. Right: Marginalized posterior contours in the w_0–w_a plane for KiDS in green, *Planck* in red, JLA SNe in purple, KiDS+*Planck* in blue and KiDS+*Planck* with informative H_0 prior in grey (from Riess et al. 2016). The dashed lines denote the ΛCDM prediction.

wider than in ΛCDM ($0.65 < h < 1.0$ at 95% CL, where the upper bound is limited by the prior) and in agreement with the Riess et al. (2016) direct measurement of H_0. The KiDS constraint on the intrinsic alignment amplitude is marginally wider than in ΛCDM, with $-0.69 < A_{IA} < 2.9$ (95% CL), and this improves to $0.13 < A_{IA} < 2.8$ (95% CL) for KiDS+*Planck*, and $0.27 < A_{IA} < 2.1$ (95% CL) for KiDS+*Planck*+H_0.

When examining the constraints in the w_0–w_a plane, KiDS is in agreement with ΛCDM, while *Planck* shows an approximately 2σ deviation from a cosmological constant. Combining KiDS+*Planck* gives an even larger deviation from the cosmological constant scenario at 3.0σ. Analogously to the constant w case (and the discussion therein), imposing a Hubble constant prior pulls the KiDS+*Planck*+H_0 contour towards ΛCDM, but the prior also helps decrease the area of the error contour such that the statistical deviation from ΛCDM is still significant at approximately 3σ (precisely, 2.7σ). This seeming preference of KiDS+*Planck* for evolving dark energy is consistent with the supernova distance measurements of the 'Joint Light-curve Analysis' sample (JLA, constructed from SDSS-II, SNLS and low-redshift samples of SN data, Betoule et al. 2013, 2014), and can be contrasted with the CFHTLenS+*Planck* scenario, where Planck Collaboration XIII (2016b) found that a Hubble constant prior is sufficient to bring the CFHTLenS+*Planck* results in agreement with ΛCDM.

Given the 3σ deviation from ΛCDM, in Fig. 11 we examine to what extent the KiDS+*Planck*+H_0 constraints in the w_0–w_a plane are consistent with the constraints from other probes combined with *Planck*. To this end, *Planck* is combined with SNe from JLA, and BAOs from the 6dF Galaxy Survey (Beutler et al. 2011), SDSS Main Galaxy Sample (Ross et al. 2015) and BOSS LOWZ/CMASS samples (Anderson et al. 2014). In the w_0–w_a plane, KiDS+*Planck*+H_0 is seemingly in tension with BAO+*Planck*, and in agreement with JLA+*Planck* (which also partly overlaps with BAO+*Planck*). While all three data combinations seem to be pulled towards $\{w_0 > -1, w_a < 0\}$, BAO+*Planck* and JLA+*Planck* are consistent with a cosmological constant at 95% CL. In this extended cosmology, the constraint on the Hubble constant from JLA+*Planck* is $0.66 < h < 0.74$ (95% CL), in agreement with the measurement from Riess et al. (2016), while the constraint from BAO+*Planck* is

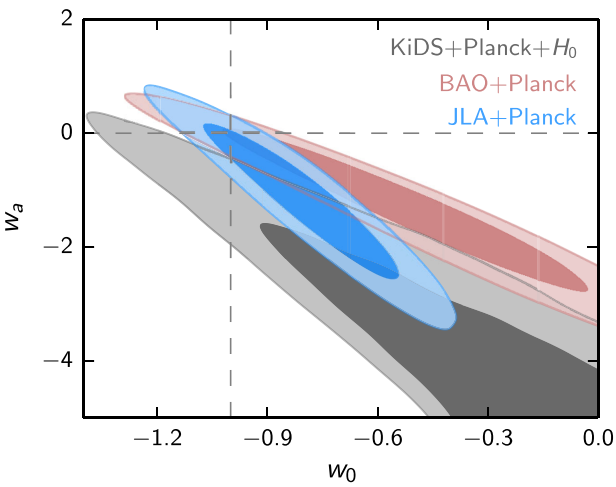

Figure 11. Marginalized posterior contours in the w_0–w_a plane (inner 68% CL, outer 95% CL) for *Planck* combined with weak lensing, BAO and SN (JLA) measurements. We show the results for KiDS+*Planck* with a $\pm5\sigma$ uniform prior on the Hubble constant from Riess et al. (2016) in grey. We show BAO+*Planck* in pink, where the BAO measurements are from 6dFGS (Beutler et al. 2011), SDSS MGS (Ross et al. 2015) and BOSS LOWZ/CMASS samples (Anderson et al. 2014). We show JLA+*Planck* in blue, where the SN measurements are from Betoule et al. (2013, 2014).

$0.59 < h < 0.69$ (95% CL), in tension with the measurement from Riess et al. (2016). Thus, it seems difficult to reconcile all the measurements simultaneously when combined with *Planck*. Meanwhile, the constraints from KIDS+BAO and KIDS+JLA are weaker, in agreement both with KiDS+*Planck*+H_0 and with a cosmological constant.

The next step is to examine to what extent the two dark energy degrees of freedom are favoured or disfavoured by the KiDS and *Planck* data sets as compared to a cosmological constant from the point of model selection. Employing again the DIC, there is no preference away from ΛCDM for KiDS and *Planck* on their own (ΔDIC = 0.95 for KiDS and ΔDIC = −1.1 for *Planck*,

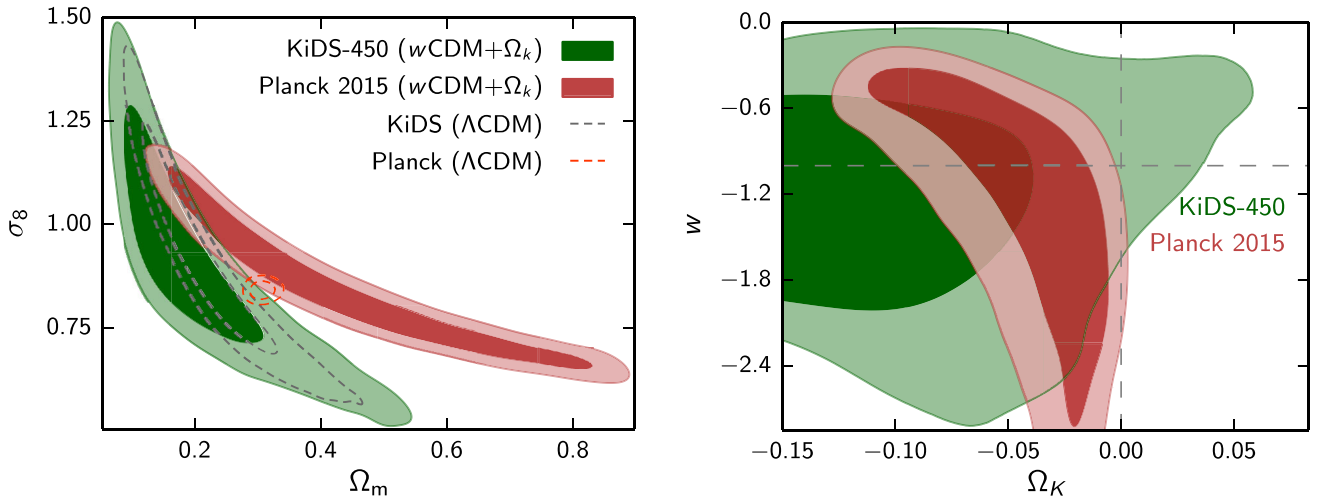

Figure 12. Left: Marginalized posterior contours in the σ_8–Ω_m plane (inner 68% CL, outer 95% CL) in a universe with both non-zero curvature and constant dark energy equation of state for KiDS in green and *Planck* in red. For comparison, dashed contours assume fiducial ΛCDM. Right: Marginalized posterior contours in the w–Ω_k plane for KiDS and *Planck* (green and red, respectively). The dashed horizontal line denotes the cosmological constant prediction, while the dashed vertical line denotes flatness.

respectively degraded from $\Delta\chi^2_{\rm eff} = -0.35$ and $\Delta\chi^2_{\rm eff} = -3.2$ due to the increased Bayesian complexity). However, when KiDS and *Planck* are combined, there is moderate preference in favour of the $w_0 - w_a$ model as compared to ΛCDM, with $\Delta{\rm DIC} = -6.4$ (marginally degraded from $\Delta\chi^2_{\rm eff} = -6.8$). In contrast to the constant w case in Section 3.4, this preference for evolving dark energy remains when further including the Riess et al. (2016) prior on the Hubble constant, such that $\Delta{\rm DIC} = -6.5$ for KiDS+*Planck*+H_0 (with similar Bayesian complexity to ΛCDM). Thus, from the point of model selection, there seems to be moderate preference in favour of the extended model when restricting the H_0 space in combining KiDS and *Planck*.

3.6 Curvature + dark energy (constant w)

In previous sections, we have considered unitary extensions to the standard cosmological model, in the form of neutrino mass, curvature and dark energy. But the impact of these extensions on the cosmological observables are often correlated (e.g. Fig. 1), and we therefore also consider a simple combination of curvature and dark energy with a constant equation of state. In other words, we simultaneously vary the curvature density parameter Ω_k and dark energy equation of state w in addition to the vanilla and lensing systematics parameters (along with the CMB degrees of freedom when applicable).

In Fig. 12, we show our constraints in the σ_8–Ω_m and w–Ω_k planes. In previous sections, we found that allowing for non-zero curvature increases the discordance between KiDS and *Planck*, while evolving dark energy increases the concordance between the data sets. In a cosmology with both Ω_k and w, the two parameters therefore partially cancel in their combined impact on the level of concordance between KiDS and *Planck*. In the σ_8–Ω_m plane, it is evident that *Planck*'s ability to constrain the matter density is further degraded as compared to the unitary curvature and dark energy extensions to ΛCDM (due to the geometric degeneracy of the CMB), stretching over large parts of the parameter space where there is no overlap with KiDS. Although the area of the KiDS contour mainly expands away from *Planck*, the two contours partly overlap for small values of the matter density and large values of σ_8. Examining the tension in the marginalized S_8 constraints, $T(S_8) = 2.5\sigma$, while accounting for the full parameter space, $\log\mathcal{I} = -0.59$, both of which are comparable to the discordance between KiDS and *Planck* in ΛCDM.

In the w–Ω_k plane, KiDS agrees with *Planck* and is concordant with the standard cosmological model, while *Planck* differs by $\gtrsim 2\sigma$ from flat ΛCDM. As the *Planck* constraint on the dark energy equation of state is weak, this is mainly driven by *Planck*'s propensity to deviate from flatness (similar to that found in Section 3.3). Weak lensing and the CMB would constitute a powerful combination, but we do not provide joint constraints on the extended degrees of freedom from KiDS and *Planck* as the two data sets are in tension. In Fig. 7, we show the *Planck* constraint on the Hubble constant in the extended cosmology. Due to the severe geometric degeneracy (given the simultaneous consideration of Ω_k and w), the Hubble constant is largely unbounded, with $0.40 < h < 0.91$ at 95% CL (pushing against the lower end of the prior). In Fig. 4, we find that the KiDS constraint on the intrinsic alignment amplitude is degraded to $-0.78 < A_{\rm IA} < 3.4$ (95% CL), increasingly consistent with no intrinsic alignments.

When examining the viability of the additional degrees of freedom from the point of model selection, KiDS shows no preference from ΛCDM (with $\Delta{\rm DIC} \approx 0$), while *Planck* weakly favours the extended cosmological model (with $\Delta{\rm DIC} = -3.7$, degraded from $\Delta\chi^2_{\rm eff} = -6.2$ due to the increase in the Bayesian complexity). This weak preference for the extended cosmological model is mainly driven by the non-zero curvature (similar to the result in Section 3.3), and is unlikely to persist with the inclusion of probes that drive the constraint on the curvature towards zero (e.g. BAOs, Planck Collaboration XIII 2016b).

3.7 Modified gravity

We now examine to what extent KiDS and *Planck* can constrain deviations from general relativity (GR), and to what extent model-independent modifications to gravity can resolve the relative discordance between these data sets (for model-independent constraints on MG using other data combinations, see e.g. Daniel et al. 2010;

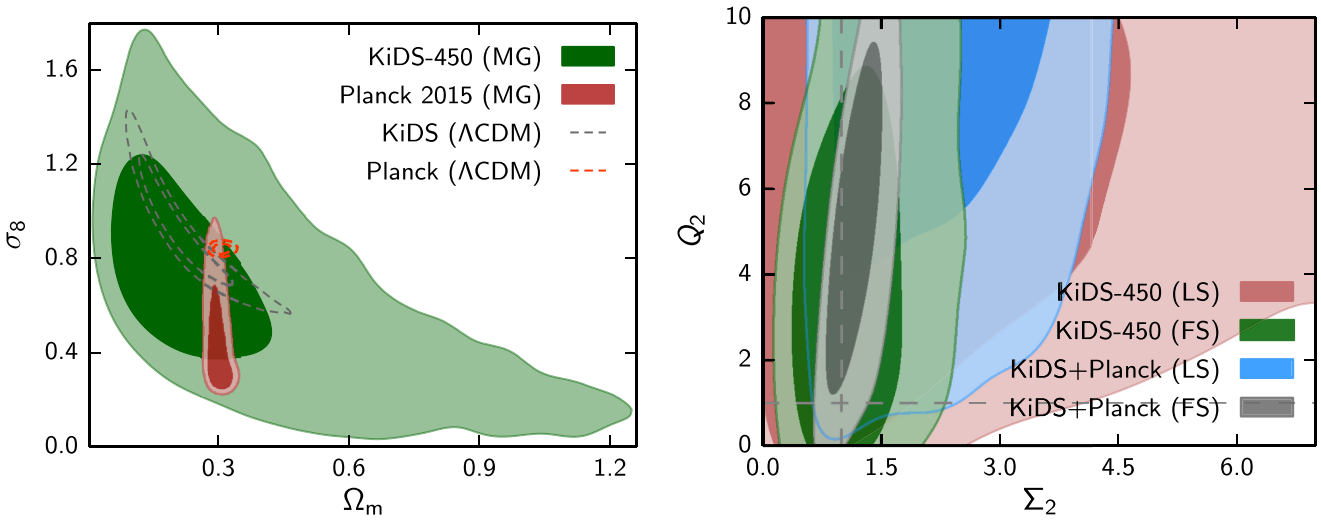

Figure 13. Left: Marginalized posterior contours in the σ_8–Ω_m plane (inner 68% CL, outer 95% CL) in a universe with MG for KiDS in green and *Planck* in red. For comparison, dashed contours assume fiducial ΛCDM. Right: Marginalized posterior contours in the Q_2–Σ_2 plane for KiDS with fiducial angular scales in green (denoted by 'FS'), KiDS keeping only the largest angular scales in pink (denoted by 'LS'), and respectively combined with *Planck* in grey and blue. The indices represent a particular combination of MG bins, such that $z < 1$ and $k > 0.05\,h\,\mathrm{Mpc}^{-1}$. The dashed lines intersect at the GR prediction ($Q = \Sigma = 1$).

Di Valentino et al. 2016a; Johnson et al. 2016; Planck Collaboration XIV 2016c). To this end, we use ISITGR (Dossett, Ishak & Moldenhauer 2011; Dossett & Ishak 2012), which is an integrated set of modified modules in COSMOMC designed to test gravity on cosmic scales.

We modify gravity in two ways. Given the first-order perturbed Einstein equations, the first modification takes the form of an effective gravitational constant that enters the Poisson equation:

$$k^2\phi = -4\pi G a^2 \sum_i \rho_i \Delta_i Q(k, a), \tag{6}$$

where ϕ is the potential describing spatial perturbations to the metric in the conformal Newtonian gauge, ρ_i is the density of species i, G is Newton's gravitational constant and $Q(k, a)$ encodes the time and scale-dependent modifications to the Poisson equation (e.g. Jain & Zhang 2008; Bean & Tangmatitham 2010; Dossett et al. 2015, also see Ma & Bertschinger 1995). The rest-frame overdensity is given by $\Delta_i \equiv \delta_i + 3Ha(1 + w_i)\theta_i/k^2$, where δ_i is the fractional overdensity, w_i is the equation of state and θ_i is the peculiar velocity divergence. Thus, we can construct an effective gravitational constant, $G_{\rm eff}(k, a) = G \times Q(k, a)$, where $Q \equiv 1$ in GR. The second modification to standard gravity enters

$$k^2[\psi - R(k, a)\phi] = -12\pi G a^2 \sum_i \rho_i \sigma_i (1 + w_i) Q(k, a), \tag{7}$$

where ψ is the potential describing temporal perturbations to the metric in the conformal Newtonian gauge, and σ_i is the anisotropic shear stress. Thus, $R(k, a)$ allows the two metric potentials to differ even in the absence of anisotropic stress, and is equivalent to unity in GR. In our MCMC calculations, we substitute R with a parameter that is more directly probed by weak lensing: $\Sigma = Q(1 + R)/2$. In general MG scenarios, the parameters Q and Σ can be functions of both scale and time, and affect the growth of structure.

We show the impact of the MG parameters on the shear correlation functions in Fig. 1, finding that the lensing observables are fairly insensitive to changes in the gravitational constant, while Σ effectively boosts or suppresses the observables uniformly across tomographic bin and angular scale unless the parameter possesses time and scale dependence. In constraining MG, we divide Q and Σ in two redshift bins and two scale bins each, with transitions at $k = 0.05\,h\,\mathrm{Mpc}^{-1}$ and $z = 1$. Thus, Q_1 and Σ_1 correspond to the {low$z$, low$k$} bins, Q_2 and Σ_2 correspond to the {low$z$, high$k$} bins, Q_3 and Σ_3 correspond to the {high$z$, low$k$} bins, Q_4 and Σ_4 correspond to the {high$z$, high$k$} bins. This results in eight MG degrees of freedom varied in our MCMC calculations in addition to the vanilla and lensing systematics parameters (along with the CMB degrees of freedom when applicable). We keep the background expansion to be that of ΛCDM. In calculating the shear correlation functions, we modify our lensing module to integrate directly over the power spectrum of the sum of the two metric potentials, which in GR reduces to the standard integration over the matter power spectrum.

In Fig. 13, we show constraints in the σ_8–Ω_m and Q_2–Σ_2 planes, where the indices represent a particular combination of MG bins, such that $z < 1$ and $k > 0.05\,h\,\mathrm{Mpc}^{-1}$. Since there exists no adequate prescription for the matter power spectrum on non-linear scales in a cosmology with binned MG (and also no screening mechanism), we consider two distinct cases: one where the fiducial angular scales of KiDS are included (described in Section 2.1), and a second case where effectively only linear scales are included in the analysis. For the latter case, we consider the same 'large-scale' cuts as in Section 3.1, removing all angular scales except for $\theta = \{24.9, 50.7\}$ arcmin in $\xi_+^{ij}(\theta)$ and $\theta = 210$ arcmin in $\xi_-^{ij}(\theta)$.

For consistency with the previous sections, we show the constraints in the σ_8–Ω_m plane for KiDS with fiducial choice of angular scales (presenting the results for KiDS with large-scale cut in Tables 2 and 3). The KiDS and *Planck* contours completely overlap, both as a result of *Planck* largely losing its ability to constrain σ_8 for a given matter density, but also because the KiDS constraints are extremely weak given the introduction of eight additional degrees of freedom. Thus, the KiDS and *Planck* S_8 constraints agree to within 1σ (for both choices of scale cuts). As shown in Table 3, when accounting for the full parameter space, $\log \mathcal{I} = 0.42$ corresponding to substantial concordance between KiDS and *Planck* when

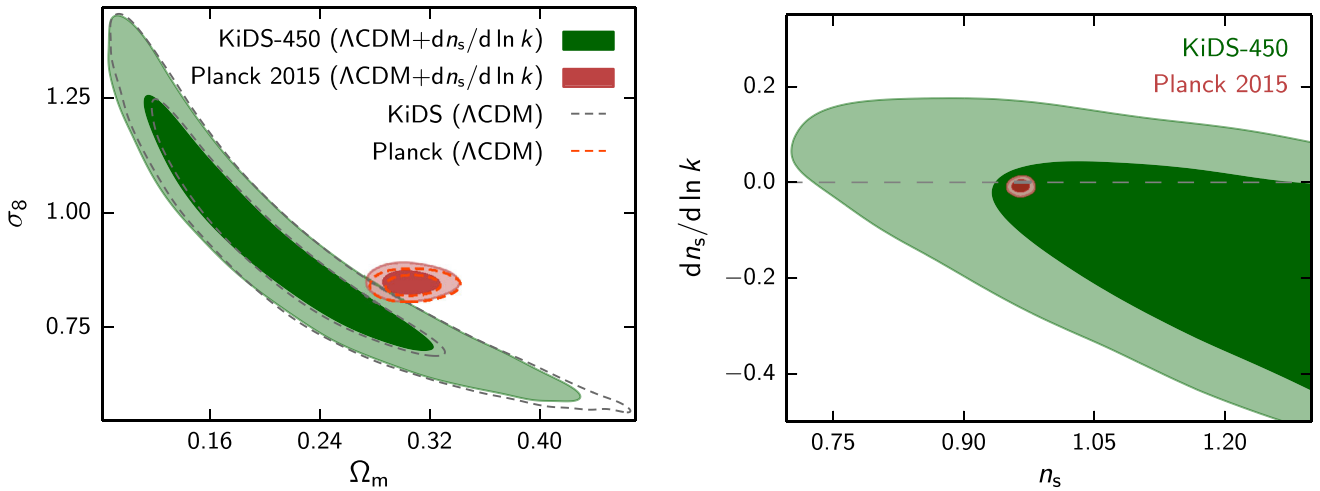

Figure 14. Left: Marginalized posterior contours in the σ_8–Ω_m plane (inner 68% CL, outer 95% CL) in a universe with non-zero running of the scalar spectral index for KiDS in green and *Planck* in red. For comparison, dashed contours assume fiducial ΛCDM. Right: Marginalized posterior contours in the $dn_s/d\ln k$–n_s plane for KiDS in green and *Planck* in red. The horizontal lines denotes the cosmology with no running of the spectral index.

considering the fiducial angular scales in KiDS, and $\log\mathcal{I} = 1.4$ corresponding to strong concordance between KiDS and *Planck* when employing large-scale cuts.

Meanwhile, as shown in Fig. 7, the Planck constraint on the Hubble constant in the extended cosmology moves marginally towards the Riess et al. (2016) result, where $0.66 < h < 0.71$ (95% CL), such that the two are still in discordance. In our MG cosmology, the intrinsic alignment amplitude is marginally pushed towards larger values (as compared to the IA amplitude in ΛCDM) such that the constraint is $-0.039 < A_{IA} < 3.1$ (95% CL) for KiDS, and $-0.033 < A_{IA} < 2.3$ (95% CL) for KiDS+*Planck*. However, the constraints degrade significantly when employing large-scale cuts, such that $-5.2 < A_{IA} < 5.1$ (95% CL) for KiDS and $-2.1 < A_{IA} < 2.5$ (95% CL) for KiDS+*Planck*. The IA amplitude constraint for KiDS with a large-scale cut in an MG cosmology can be contrasted with the corresponding constraint in ΛCDM, which at $-5.0 < A_{IA} < 3.2$ (95% CL) is also fully consistent with zero.

In the Q_2–Σ_2 plane, the KiDS constraints are consistent with GR, and mainly sensitive to Σ_2 as expected. The MG constraints from KiDS are weak for most of the MG parameters, and significantly degraded when keeping only large angular scales, given the significant reduction in the size of the data vector and information contained in the KiDS measurements. The agreement with GR persists when combining KiDS with *Planck*, not only for Q_2 and Σ_2, but for the other MG parameters as well, where the constraints on Σ_i are significantly tighter than the constraints on Q_i, for both choices of scale cuts (often by an order of magnitude). As shown in Fig. B1, the minor exception to the GR agreement is $Q_2 > 2.2$ (at 95% CL, which reduces to 0.84 at 99% CL) for KiDS+*Planck* where a large-scale cut is employed.

Given our particular model of MG, the goodness of fit improves moderately as compared to GR (with $\Delta\chi^2_{\rm eff} \approx -4$ for both KiDS and *Planck*, and their joint analysis when fiducial angular scales are considered, and by $\Delta\chi^2_{\rm eff} \approx -6$ when large-scale cuts are employed), but this is understandable given the introduction of eight additional degrees of freedom. When examining the difference in DIC between our MG model and GR, we find no preference in favour of MG (with $\Delta{\rm DIC} \approx 6$ for Planck, $\Delta{\rm DIC} \approx 0$ for KiDS and KiDS+Planck when fiducial scales are considered, $\Delta{\rm DIC} \approx 6$ for KiDS with a large-scale cut, and $\Delta{\rm DIC} \approx 2$ for KiDS+*Planck* with a large-scale cut). A next step would be to consider more model-dependent approaches to constraining MG, but we leave further investigations of these models and their potential viability to forthcoming analyses.

3.8 Running of the spectral index

Lastly, beyond the curvature of the universe, we also relax the strong inflation prior on the running of the scalar spectral index, $dn_s/d\ln k$, defined via the dimensionless power spectrum of primordial curvature perturbations,

$$\ln P_s(k) = \ln A_s + (n_s - 1)\ln\left(\frac{k}{k_{\rm pivot}}\right) + \frac{1}{2}\frac{dn_s}{d\ln k}\ln\left(\frac{k}{k_{\rm pivot}}\right)^2, \quad (8)$$

where A_s, n_s and $dn_s/d\ln k$ are evaluated at the pivot wavenumber $k_{\rm pivot}$ listed in Table 1. While most popular inflation models predict $|dn_s/d\ln k| \lesssim 10^{-3}$ (Kosowsky & Turner 1995), large negative running can be generated by multiple fields, temporary breakdown of slow-roll or several distinct inflationary stages (e.g. Baumann et al. 2009 and references therein).

In Fig. 1, we show the imprint of a non-zero running of the scalar spectral index on the lensing observables. As expected, through its impact on the matter power spectrum, a negative running provides a scale-dependent suppression of the shear correlation functions that increases towards small angular scales, and is particularly correlated with the imprint of baryon feedback. We show the resulting constraints in the σ_8–Ω_m and $dn_s/d\ln k$–n_s planes in Fig. 14. In the σ_8–Ω_m plane, it is evident that the introduction of non-zero running does not alleviate the tension between KiDS and *Planck*, with the respective contours only marginally affected by the extended degree of freedom. Analogous to the ΛCDM results, the tension in the S_8 parameter is at the 2.3σ level, and $\log\mathcal{I} = -0.66$ corresponding to 'substantial discordance' between the KiDS and *Planck* data sets.

When examining the constraints in the $dn_s/d\ln k$–n_s plane, we find weak constraints on both parameters from KiDS. However, KiDS does independently from *Planck* agree with zero running of the scalar spectral index (marginalized constraint of $-0.40 < dn_s/d\ln k < 0.15$ at 95% CL). As expected, the *Planck*

constraint on the running is substantially more competitive, and would require significantly more precise lensing measurements to improve. Meanwhile, in the extended cosmology, the *Planck* constraint on the Hubble constant and the KiDS constraint on the intrinsic alignment amplitude are both close to the respective constraints in ΛCDM. The extended cosmology does not improve the goodness of fit noticeably as compared to ΛCDM (with $\Delta\chi^2_{\rm eff} \approx -1$ for KiDS and $\Delta\chi^2_{\rm eff} \approx 0$ for *Planck*), and is not favoured by the KiDS and *Planck* data sets (with $\Delta{\rm DIC} \lesssim 1$ for KiDS and *Planck*).

4 CONCLUSIONS

We have performed an extended lensing systematics and cosmology analysis of the tomographic weak gravitational lensing measurements of the KiDS (de Jong et al. 2013; Kuijken et al. 2015; Hildebrandt et al. 2017). The extended lensing systematics include non-informative priors on the amplitude and redshift dependence of intrinsic galaxy alignments, and baryonic feedback modifying the non-linear matter power spectrum. In Appendix A, we further explore the impact of increasing our uncertainty on either the shear calibration correction, or the photometric redshift distributions, or indeed any systematic that changes the amplitude of the weak lensing signal. Meanwhile, the extended cosmologies with fiducial treatment of the systematic uncertainties include massive neutrinos, non-zero curvature, evolving dark energy, MG and running of the spectral index. The aim of this paper has been three-fold. We have examined to what extent the extended models can be constrained by KiDS, to what extent they are favoured as compared to the standard cosmological model, and to what extent they can alleviate the discordance between KiDS and *Planck* CMB temperature measurements.

To this end, we use the same KiDS measurements, fitting pipeline and approach to systematic uncertainties as in Hildebrandt et al. (2017). In addition to the standard ΛCDM parameters, we always vary the intrinsic alignment and baryon feedback amplitudes (fiducially with informative priors). We do not vary any parameters in our treatment of the photometric redshift uncertainties, but instead capture the uncertainties with 1000 bootstrap realizations of the tomographic redshift distributions. Unlike Hildebrandt et al. (2017), we do not fiducially impose an informative prior on the Hubble constant from Riess et al. (2016), which extends our contours along the lensing degeneracy direction but does not particularly affect the discordance with *Planck*.

In a ΛCDM cosmology with fiducial treatment of lensing systematics, the discordance between KiDS and *Planck* is 2.1σ in $S_8 = \sigma_8(\Omega_{\rm m}/0.3)^{0.5}$. In evaluating the level of discordance over the full parameter space, we use the $\log\mathcal{I}$ statistic grounded in information theory. Similar to the result in Hildebrandt et al. (2017), we find $\log\mathcal{I} = -0.63$, which corresponds to 'substantial discordance' between the two data sets. As we move beyond the fiducial model, our findings are summarized below:

(i) *Extended lensing systematics*: We impose non-informative priors on the intrinsic alignment and baryon feedback amplitudes ($A_{\rm IA}$ and B), and introduce $\eta_{\rm IA}$ that governs the redshift dependence of the intrinsic alignment signal. These parameters are constrained to $B < 4.6$ (95% CL), $-0.45 < A_{\rm IA} < 2.3$ (95% CL) and $-16 < \eta_{\rm IA} < 4.7$ (95% CL). The constraints are consistent with the fiducial treatment of lensing systematics, and do not particularly affect the discordance between KiDS and *Planck*. The discordance between the data sets remains even when removing the smallest angular scales in KiDS most sensitive to non-linear physics, or allowing for a large uncertainty in the amplitudes of the shear correlation functions bin due to unknown systematics. As we step through each of the extended cosmologies below, the KiDS constraint on the intrinsic alignment amplitude is remarkably robust with a consistent 2σ positive deviation from zero.

(ii) *Neutrino mass*: We capture the effects of neutrino mass on the non-linear matter power spectrum with an updated version of HMCODE (Mead et al. 2016). KiDS constrains $\sum m_\nu < 4.0$ eV (95% CL), which does not bring about concordance between KiDS and *Planck*, and is not required by the data.

(iii) *Curvature*: KiDS and *Planck* independently constrain the curvature to be positive at about 95% CL. Employing model selection criteria, non-zero curvature is not favoured by KiDS, and weakly favoured by *Planck*. The extra degree of freedom increases the discordance between the data sets to 3.5σ in S_8, and to $\log\mathcal{I} = -1.7$ (corresponding to 'strong discordance').

(iv) *Dark energy (constant* w*)*: A constant dark energy equation of state w brings 'substantial-to-strong' concordance between KiDS and *Planck*. In this cosmology, the *Planck* constraint on the Hubble constant is wider and in agreement with Riess et al. (2016). KiDS and *Planck* are separately in agreement with a cosmological constant, but the combined analysis of KiDS and *Planck* with a uniform prior on H_0 from Riess et al. (2016) deviates by 2σ from $w = -1$. From the point of model selection, the extended model is weakly favoured as compared to ΛCDM.

(v) *Dark energy (*$\rm w_0 - w_a$*)*: A time-dependent parametrization of the dark energy equation of state brings substantial concordance between KiDS and *Planck*, and removes the H_0 tension between *Planck* and Riess et al. (2016). KiDS is in agreement with a cosmological constant, while *Planck* shows a 2σ deviation. Combining KiDS and *Planck* with a uniform H_0 prior from Riess et al. (2016) gives a 3σ deviation from a cosmological constant that is moderately favoured by the data. This deviation from a cosmological constant is consistent with SN distance measurements from the JLA (Betoule et al. 2013, 2014), but in tension with BAO measurements from the 6dF Galaxy Survey (Beutler et al. 2011), SDSS Main Galaxy Sample (Ross et al. 2015) and BOSS LOWZ/CMASS samples (Anderson et al. 2014) when combined with *Planck*. Meanwhile, the BAO+*Planck* constraints are separately in tension with Riess et al. (2016). The constraints from KiDS+JLA and KiDS+BAO are weaker, in agreement both with KiDS+*Planck*+H_0 and with a cosmological constant.

(vi) *Curvature + dark energy (constant* w*)*: Beyond unitary extensions to the underlying cosmology, we simultaneously vary Ω_k and w. The impacts of the two degrees of freedom partially cancel, such that the discordance between KiDS and *Planck* is similar to that in ΛCDM. The extra degrees of freedom are only weakly constrained by KiDS, and not favoured by the data.

(vii) *Modified gravity*: Introducing parameters that govern deviations to the Poisson equation $Q(k, a)$ and deflection of light $\Sigma(k, a)$, divided in two redshift bins and two scale bins each, removes the discordance between KiDS and *Planck*. However, the extra degrees of freedom are not favoured by the data, and the MG constraints are in agreement with GR.

(viii) *Running of the spectral index*: The KiDS/*Planck* discordance is only marginally affected by a running of the spectral index. Independently from other probes, KiDS constrains the running to be consistent with zero ($-0.40 < {\rm d}n_{\rm s}/{\rm d}\ln k < 0.15$ at 95% CL).

To conclude, the discordance between KiDS and *Planck* is largely robust to changes in the lensing systematics and underlying cosmology. The most interesting exception to this is a cosmology

with a time-dependent dark energy equation of state, which provides substantial concordance between KiDS and *Planck*, is 3σ discrepant from the cosmological constant scenario and is moderately favoured by KIDS+*Planck*. The KiDS data are publicly available at http://kids.strw.leidenuniv.nl. We also make the fitting pipeline and data that were used in this analysis public at https://github.com/sjoudaki/kids450.

ACKNOWLEDGEMENTS

We much appreciate useful discussions with Alexandre Barreira, Jason Dossett, Manoj Kaplinghat, Antony Lewis, Nikhil Padmanabhan, David Parkinson and Martin White. We thank Simon Forsayeth, Robin Humble and Jarrod Hurley for HPC support. We also thank George Efstathiou for useful discussions about internal consistency tests, and the anonymous referee for their helpful comments on this paper. We acknowledge the use of ASTAC and CAASTRO time on Swinburne's swinSTAR and NCI's Raijin machines. We acknowledge the use of CAMB and COSMOMC packages (Lewis et al. 2000; Lewis & Bridle 2002). This work is based on data products from observations made with ESO Telescopes at the La Silla Paranal Observatory under programme IDs 177.A-3016, 177.A-3017 and 177.A-3018. Parts of this research were conducted by the Australian Research Council Centre of Excellence for All-sky Astrophysics (CAASTRO), through project number CE110001020. This work was supported by the Flagship Allocation Scheme of the NCI National Facility at the ANU. This work was performed in part at the Aspen Center for Physics, which is supported by National Science Foundation grant PHY-1066293. AM acknowledges support from a CITA National Fellowship. CB acknowledges the support of the Australian Research Council through the award of a Future Fellowship. AC acknowledges support from the European Research Council under the FP7 grant number 240185. JdJ is supported by the Netherlands Organisation for Scientific Research (NWO) through grant 614.061.610. IFC acknowledges the use of computational facilities procured through the European Regional Development Fund, Project ERDF-080 'A supercomputing laboratory for the University of Malta'. CH acknowledges support from the European Research Council under grant numbers 240185 and 647112. HHi is supported by an Emmy Noether grant (No. Hi 1495/2-1) of the Deutsche Forschungsgemeinschaft. HHo acknowledges support from the European Research Council under FP7 grant number 279396. BJ acknowledges support by an STFC Ernest Rutherford Fellowship, grant reference ST/J004421/1. DK and PS are supported by the Deutsche Forschungsgemeinschaft in the framework of the TR33 'The Dark Universe'. FK acknowledges support from a de Sitter Fellowship of the Netherlands Organization for Scientific Research (NWO) under grant number 022.003.013. KK acknowledges support by the Alexander von Humboldt Foundation. LM is supported by STFC grant ST/N000919/1. MV acknowledges support from the European Research Council under FP7 grant number 279396 and the Netherlands Organisation for Scientific Research (NWO) through grant 614.001.103.

REFERENCES

Addison G. E., Huang Y., Watts D. J., Bennett C. L., Halpern M., Hinshaw G., Weiland J. L., 2016, ApJ, 818, 132
Alsing J., Heavens A. F., Jaffe A. H., 2017, MNRAS, 466, 3272
Anderson L. et al., 2014, MNRAS, 441, 24
Archidiacono M., Gariazzo S., Giunti C., Hannestad S., Hansen R., Laveder M., Tram T., 2016, J. Cosmol. Astropart. Phys., 8, 067
Battye R. A., Charnock T., Moss A., 2015, Phys. Rev. D, 91, 103508
Baumann D. et al., 2009, AIP Conf. Proc. Vol. 1141, CMB Polarization Workshop: Theory and Foregrounds: CMB Pol Mission Concept Study. Am. Inst. Phys., New York, p. 10
Bean R., Tangmatitham M., 2010, Phys. Rev. D, 81, 083534
Begeman K., Belikov A. N., Boxhoorn D. R., Valentijn E. A., 2013, Exp. Astron., 35, 1
Benítez N., 2000, ApJ, 536, 571
Bernal J. L., Verde L., Riess A. G., 2016, J. Cosmol. Astropart. Phys., 019
Betoule M. et al., 2013, A&A, 552, A124
Betoule M. et al., 2014, A&A, 568, A22
Beutler F. et al., 2011, MNRAS, 416, 3017
Bird S., Viel M., Haehnelt M. G., 2012, MNRAS, 420, 2551
Burles S., Nollett K. M., Turner M. S., 2001, Phys. Rev. D, 63, 063512
Calabrese E. et al., 2013, Phys. Rev. D, 87, 103012
Chevallier M., Polarski D., 2001, Int. J. Mod. Phys. D, 10, 213
Cyburt R. H., Fields B. D., Olive K. A., Yeh T.-H., 2016, Rev. Mod. Phys., 88, 015004
de Jong J. T. A., Verdoes Kleijn G. A., Kuijken K. H., Valentijn E. A., 2013, Exp. Astron., 35, 25
de Jong J. T. A. et al., 2015, A&A, 582, A62
Di Valentino E., Melchiorri A., Silk J., 2016a, Phys. Rev. D, 93, 023513
Di Valentino E., Melchiorri A., Silk J., 2016b, Phys. Lett. B, 761, 242
Daniel S. F., Linder E. V., Smith T. L., Caldwell R. R., Cooray A., Leauthaud A., Lombriser L., 2010, Phys. Rev., D81, 123508
Dossett J. N., Ishak M., 2012, Phys. Rev. D, 86, 103008
Dossett J. N., Ishak M., Moldenhauer J., 2011, Phys. Rev. D, 84, 123001
Dossett J. N., Ishak M., Parkinson D., Davis T. M., 2015, Phys. Rev. D, 92, 023003
Enqvist K., Nadathur S., Sekiguchi T., Takahashi T., 2015, J. Cosmol. Astropart. Phys., 9, 067
Erben T. et al., 2013, MNRAS, 433, 2545
Fenech-Conti I., Herbonnet R., Hoekstra H., Merten J., Miller L., Viola M., 2017, MNRAS, 467, 1627
Gelman A., Rubin D., 1992, Stat. Sci., 7, 457
Grandis S., Rapetti D., Saro A., Mohr J. J., Dietrich J. P., 2016, MNRAS, 463, 1416
Hall A. C., Challinor A., 2012, MNRAS, 425, 1170
Heitmann K., Lawrence E., Kwan J., Habib S., Higdon D., 2014, ApJ, 780, 111
Heymans C. et al., 2012, MNRAS, 427, 146
Hildebrandt H. et al., 2012, MNRAS, 421, 2355
Hildebrandt H. et al., 2017, MNRAS, 465, 1454
Hirata C. M., Seljak U., 2004, Phys. Rev. D, 70, 063526
Jain B., Seljak U., 1997, ApJ, 484, 560
Jain B., Zhang P., 2008, Phys. Rev. D, 78, 063503
Jee M. J., Tyson J. A., Hilbert S., Schneider M. D., Schmidt S., Wittman D., 2016, ApJ, 824, 77
Jeffreys H., 1961, Theory of Probability, 3rd edn, Oxford Classics series (reprinted 1998). Oxford Univ. Press, Oxford
Joachimi B., Mandelbaum R., Abdalla F. B., Bridle S. L., 2011, A&A, 527, A26
Johnson A., Blake C., Dossett J., Koda J., Parkinson D., Joudaki S., 2016, MNRAS, 458, 2725
Joudaki S., 2013, Phys. Rev. D, 87, 083523
Joudaki S., Kaplinghat M., 2012, Phys. Rev. D, 86, 023526
Joudaki S. et al., 2017, MNRAS, 465, 2033
Karwal T., Kamionkowski M., 2016, Phys. Rev. D, 94, 103523
Kass R. E., Raftery A. E., 1995, J. Am. Stat. Assoc., 90, 773
Kilbinger M. et al., 2013, MNRAS, 430, 2200
Köhlinger F., Viola M., Valkenburg W., Joachimi B., Hoekstra H., Kuijken K., 2016, MNRAS, 456, 1508
Komatsu E. et al., 2009, ApJS, 180, 330
Kosowsky A., Turner M. S., 1995, Phys. Rev. D, 52, R1739
Kuijken K. et al., 2015, MNRAS, 454, 3500

Kunz M., Trotta R., Parkinson D. R., 2006, Phys. Rev. D, 74, 023503
Kunz M., Nesseris S., Sawicki I., 2015, Phys. Rev. D, 92, 063006
Le Brun A. M. C., McCarthy I. G., Schaye J., Ponman T. J., 2014, MNRAS, 441, 1270
Leistedt B., Peiris H. V., Verde L., 2014, Phys. Rev. Lett., 113, 041301
Lewis A., Bridle S., 2002, Phys. Rev. D, 66, 103511
Lewis A., Challinor A., Lasenby A., 2000, ApJ, 538, 473
Liddle A. R., 2007, MNRAS, 377, L74
Linder E. V., 2003, Phys. Rev. Lett., 90, 091301
Liu J., Ortiz-Vazquez A., Hill J. C., 2016, Phys. Rev. D, 93, 103508
MacCrann N., Zuntz J., Bridle S., Jain B., Becker M. R., 2015, MNRAS, 451, 2877
MacCrann N. et al., 2017, MNRAS, 465, 2567
Ma C.-P., Bertschinger E., 1995, ApJ, 455, 7
Marshall P., Rajguru N., Slosar A., 2006, Phys. Rev. D, 73, 067302
Massara E., Villaescusa-Navarro F., Viel M., 2014, J. Cosmol. Astropart. Phys., 12, 053
Mead A. J., Peacock J. A., Heymans C., Joudaki S., Heavens A. F., 2015, MNRAS, 454, 1958
Mead A. J., Heymans C., Lombriser L., Peacock J. A., Steele O. I., Winther H. A., 2016, MNRAS, 459, 1468
Miller L. et al., 2013, MNRAS, 429, 2858
Natarajan A., Zentner A. R., Battaglia N., Trac H., 2014, Phys. Rev. D, 90, 063516
Olive K. A., Particle Data Group, 2014, Chin. Phys. C, 38, 090001
Planck Collaboration XVI, 2014, A&A, 571, A16
Planck Collaboration XI, 2016a, A&A, 594, A11
Planck Collaboration XIII, 2016b, A&A, 594, A13
Planck Collaboration XIV, 2016c, A&A, 594, A14
Planck Collaboration LI, 2016d, preprint (arXiv:1608.02487)
Raveri M., 2016, Phys. Rev., D93, 043522
Riess A. G. et al., 2011, ApJ, 730, 119
Riess A. G. et al., 2016, ApJ, 826, 56
Ross A. J., Samushia L., Howlett C., Percival W. J., Burden A., Manera M., 2015, MNRAS, 449, 835
Schaye J. et al., 2010, MNRAS, 402, 1536
Semboloni E., Hoekstra H., Schaye J., van Daalen M. P., McCarthy I. G., 2011, MNRAS, 417, 2020
Semboloni E., Hoekstra H., Schaye J., 2013, MNRAS, 434, 148
Spiegelhalter D., Best N. G., Carlin B. P., 2002, J. R. Stat. Soc. B, 64, 583
Spiegelhalter D., Best N. G., Carlin B. P., van der Linde A., 2014, J. R. Stat. Soc. B, 76, 485
Springel V., 2005, MNRAS, 364, 1105
Takahashi R., Sato M., Nishimichi T., Taruya A., Oguri M., 2012, ApJ, 761, 152
The Dark Energy Survey Collaborations, 2016, Phys. Rev. D, 94, 022001
Trotta R., 2008, Contemp. Phys., 49, 71
van Daalen M. P., Schaye J., Booth C. M., Dalla Vecchia C., 2011, MNRAS, 415, 3649

APPENDIX A: IMPACT OF UNKNOWN SYSTEMATICS

As with all scientific analyses we cannot categorically rule out that there are additional unknown sources of systematic uncertainties that have not been considered in our analysis (take for example the 'GI' intrinsic alignment term that is now considered, but was unknown to the weak lensing community until Hirata & Seljak 2004). To explore the impact of increasing our uncertainty on either the shear calibration correction, or the photometric redshift distributions, or indeed any systematic that changes the amplitude of the weak lensing signal, we show in Fig. A1 the submatrix of constraints on the amplitudes $\mathcal{U}_i$ in each of the four tomographic bins such that $\xi_\pm^{ij}(\theta) \rightarrow (1+\mathcal{U}_i)(1+\mathcal{U}_j)\xi_\pm^{ij}(\theta)$ with Gaussian priors arbitrarily chosen to have a width $\sigma(\mathcal{U}_i) = 0.05$. These additional nuisance parameters can be compared to the constraints on the intrinsic alignment amplitude, the baryonic feedback parameter and the derived $S_8 = \sigma_8\sqrt{\Omega_\mathrm{m}/0.3}$ parameter. We do not show constraints on the primary ΛCDM parameters, which are simultaneously varied in the analysis. Despite the wide priors on the $\mathcal{U}_i$ parameters, there is only a 15 per cent increase in the uncertainty on S_8. We find $S_8 = 0.756 \pm 0.046$ in the extended analysis as compared to $S_8 = 0.752 \pm 0.040$ in the fiducial analysis. In this, rather arbitrary, case the discordance with *Planck* would decrease by 0.3σ (such that the tension is still at the 2σ level).

This test both verifies the Fisher matrix analysis in appendix A of Hildebrandt et al. (2017), and allows us to look for internal consistency between the different tomographic slices. We find that the constraints on $\mathcal{U}_i$ are dominated by the prior, with the posterior means all consistent with zero such that the tomographic slices are consistent with each other. The largest amplitude shift can be seen in the third tomographic bin where the lensing measurements are comparably lower than the other tomographic bins. The likely cause of this slight amplitude change is the presence of small-angular scale, low amplitude B-modes that predominantly affect the third tomographic bin (Hildebrandt et al. 2017).

We find that the fit to the data does not particularly improve when including these four additional degrees of freedom, and the change in $\Delta\mathrm{DiC} \approx 5$, such that this extended unknown systematics model is not favoured by the data.

APPENDIX B: MODIFIED GRAVITY SUBSPACE

In Fig. B1, we show the submatrix of binned MG constraints obtained in the analysis presented in Section 3.7.

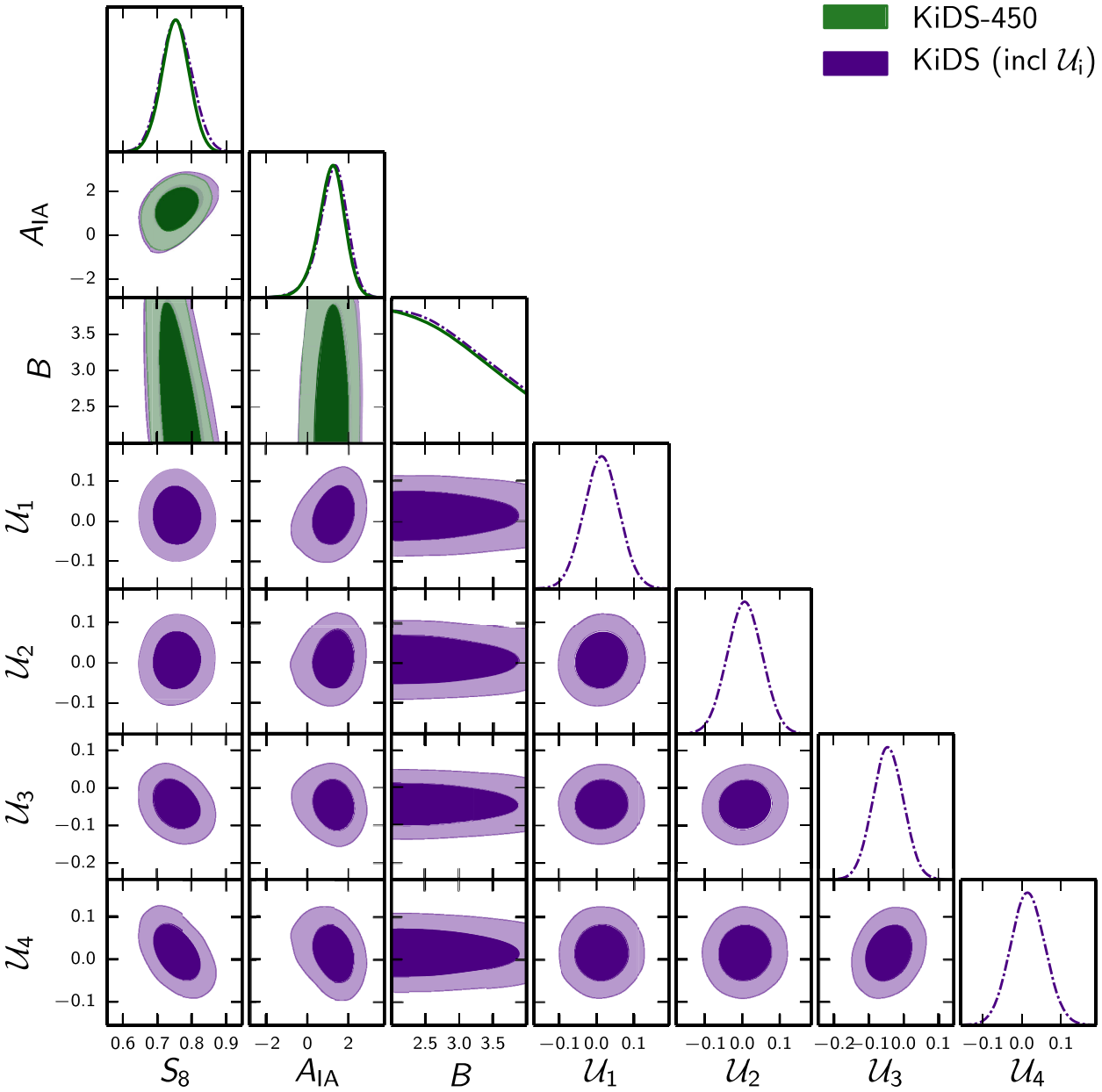

Figure A1. Posterior distributions of the $S_8 = \sigma_8\sqrt{\Omega_m/0.3}$ parameter combination, intrinsic alignment amplitude A_{IA}, baryon feedback B, unknown sources of systematic amplitudes $\mathcal{U}_i$ and their correlation. The constraints in green (solid) correspond to the fiducial KiDS analysis, where $\mathcal{U}_i = 0$, while the constraints in purple vary the $\mathcal{U}_i \in (-0.3, 0.3)$ with Gaussian priors of $\sigma(\mathcal{U}_i) = 0.05$ along with the other parameters. The priors on other parameters are listed in Table 1. In this figure, we do not show the primary ΛCDM parameters that were simultaneously varied in the MCMC.

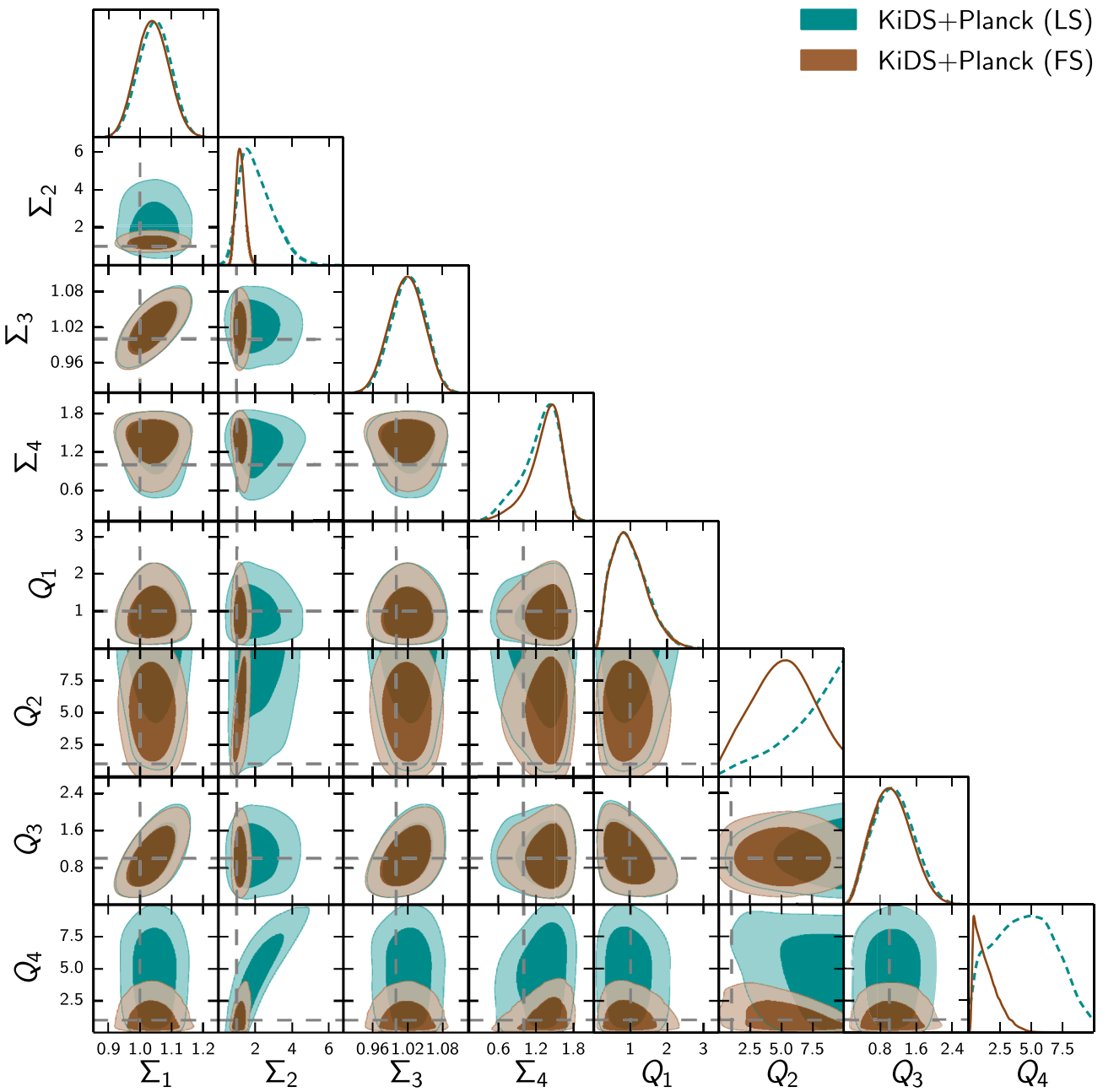

Figure B1. Posterior distributions of the MG parameters and their correlation. The constraints in brown (solid) correspond to KiDS+*Planck*, considering the fiducial angular scales of KiDS (listed in Section 2.1), while the constraints in cyan (dashed) correspond to KiDS+*Planck* keeping only the largest, effectively linear, scales of KiDS (Section 3.7). Parameter definitions and priors are listed in Table 1. The bin transitions are at $k = 0.05\,h\,\mathrm{Mpc}^{-1}$ and $z = 1$. The indices are devised such that Q_1 and Σ_1 correspond to the $\{\mathrm{low}\,z, \mathrm{low}\,k\}$ bins, Q_2 and Σ_2 correspond to the $\{\mathrm{low}\,z, \mathrm{high}\,k\}$ bins, Q_3 and Σ_3 correspond to the $\{\mathrm{high}\,z, \mathrm{low}\,k\}$ bins, Q_4 and Σ_4 correspond to the $\{\mathrm{high}\,z, \mathrm{high}\,k\}$ bins. GR is given by $Q = \Sigma = 1$. In this figure, we do not show the other fiducial lensing and CMB parameters that were simultaneously varied in the MCMC.

This paper has been typeset from a TEX/LATEX file prepared by the author.